Novel nanostructures for guided mode resonance in tungsten disulphide

YASH KUMAR DESAI

Master's by Research

University of York

School of Physics, Engineering and Technology

December 2025

Abstract

Two-dimensional (2D) materials have emerged as a versatile platform for next-generation photonic and optoelectronicdevices due to their unique optical, electrical, and physical properties. In contrast to conventional bulk high–refractive-index dielectric materials, 2D materials offer strong light–matter interaction, excitonic effects, and tunability, opening new opportunities for nanophotonic device engineering. Among them, tungsten disulfide (WS_2), a transition metal dichalcogenide (TMD), is an emerging semiconductor with significant potential for advanced device architectures owing to its excellent optical response and compatibility with nanoscale fabrication techniques.

In this work, we explore the fabrication and optical characterization of one-dimensional grating nanostructures in WS_2 as part of a master's research project. WS_2 flakes were prepared using mechanical exfoliation followed by dry transfer onto the target substrate. Electron-beam lithography (EBL) was employed to define periodic 1D grating patterns with varying periods. Optical measurements reveal clear resonant features, with a peak wavelength of approximately 742 nm and a quality factor (Q) of 46 for a grating period of 260 nm. These experimental results show good agreement with simulation.

The demonstrated WS_2 grating structures highlight the potential of nanophotonic architectures based on 2D TMD for applications in optical sensing, integrated photonics, metasurfaces, and light–matter interaction engineering. More broadly, this work contributes to the growing field of 2D material–based photonics, which leverages strong excitonic effects, nonlinear optical responses, high reflective index and low loss and nanoscale confinement to enable novel hybrid photonic devices across a wide spectral range.

Acknowledgements

I am deeply grateful to my supervisor, **Dr Christina Wang**, for welcoming me into her research group and for providing continuous guidance and support throughout my PhD. I sincerely appreciate the freedom she gave me to explore new ideas, learn independently, and grow as a researcher.

I would like to thank **Dr David Dickinson** for being an enthusiastic and supportive member of my Thesis Advisory Panel. I am also thankful to Professor Thomas F. Krauss and Professor Steven G. Johnson for their valuable insights and constructive feedback during group discussions.

I am extremely grateful for the friendship, encouragement, and support of the past and present members of the Photonics Group. In particular, I would like to thank Dr Chris Reardon, Dr Sam Blair, and Dr Josh Male and Dr Augusto Martins for their invaluable help and advice in problem-solving. I would also like to thank my colleagues Dr Francisca D'Rozario, Dr Pin Dong, Dr Alexander Drayton, Minahil Khan, Dr Soheila Kharratian, Dr Kezheng Li, Dr Lisa Miller, Dr Callum Silver, Adam Stroughair, Katie Thornton, Dr Katie Morris, Ayesha Razi, and Timothy Woodford, Dan Mitchell for creating a supportive and stimulating research environment.

I would like to extend special thanks to Dr Richard John for providing essential laboratory training and for his assistance whenever needed. I am also grateful to Dr Fahrettin Sarcan, Associate Professor at Istanbul University, for his support with experimental procedures.

I would like to thank my family—my father **Girishbhai**, my mother **Madhuben**, my sister **Palak**, my grandfather **Chhaganbhai**, and the newest member of our family, **Raha**—for their constant love, encouragement, and support. I am especially thankful to my friends, particularly **Sharada**, for their motivation during difficult times. I would also like to express my heartfelt gratitude to Miss **Jyoti** for her loving support and encouragement throughout challenging periods.

Finally, I would like to thank the University of York for providing me with the opportunity to pursue this research and for offering excellent facilities and resources.

Declaration of Authorship

I declare that this thesis is a presentation of original work and I am the sole author.This work has not previously been presented for a degree or other qualification at this University or elsewhere. All sources are acknowledged as references.

Contents

List of Figures

Chapter 1

Introduction

1.1 Motivation

Intense research on two-dimensional (2D) materials was sparked in 2004 by the isolation of single-layer graphene and the discovery of its unique photonic properties[3]. This breakthrough introduced the technique of exfoliation, which was quickly applied to other materials composed of atomic layers held together by relatively weak van der Waals (vdW) forces. By stacking these layers together, heterostructures were created[4], and the introduction of a relative twist angle between the layers produced moiré patterns, further expanding the range of properties of 2D materials[5]. These fabrication techniques, together with the rapidly expanding library of exfoliable materials such as graphene, hexagonal boron nitride(hBN), and transition metal dichalcogenides(TMDs), form the backbone of the rapidly growing field of 2D materials. The exceptional optical properties of 2D materials include strong light–matter interaction, tunable direct bandgaps, pronounced excitonic effects, large nonlinear responses, and broadband optical absorption. For example, monolayer TMDs such as MoS_2 and WS_2 exhibit direct bandgaps in the visible range ($\sim$ 1.8–2.1 eV), with exciton binding energies on the order of hundreds of meV, leading to stable excitonic resonances even at room temperature. Because of the exceptional optical properties of these materials, photonics occupies a prominent position within this field, where they have generated high expectations for the discovery of new phenomena and the development of groundbreaking applications.

Among TMDs, tungsten disulfide ($\mathbf{WS_2}$) is of particular interest due to its strong excitonic oscillator strength, high photoluminescence quantum yield, and relatively large spin–orbit coupling ($\sim$ 400 meV in the valence band), in monolayer of WS_2 which enables valley selective optical responses. In contrast, bulk WS_2 possesses an indirect band gap due to interlayer coupling, leading to reduced photoluminescence efficiency and weaker excitonic effects compared to the monolayer. The restoration of inversion symmetry in the bulk suppresses valley-selective optical responses and spin valley coupling. Nevertheless, bulk WS_2 maintains strong optical absorption and a high refractive index, making it suitable for thickness-dependent light–matter interaction in photonic structures. These characteristics make WS_2 an excellent candidate for enhancing light–matter interaction in resonant photonic structures.

Appealing properties of 2D material and their heterostructures[6] are :

- Strong Optical Confinement. The in-plane wavelength of polaritonic modes is much smaller than that of light, enabling small, laterally structured 2D materials to be optically resonant.
- Broad Spectral Range. 2D polaritons, and material excitations in general, span a wide range of frequencies, extending from the terahertz (THz) domain to the visible and ultraviolet (UV), and acquiring the form of plasmons (e.g., in graphene and thin metals), phonons (e.g., in ionic crystals such as (hBN) and MoO_3), and excitons (e.g., in TMDs).
- Long Lifetime. Graphene plasmons and phonon polaritons in the mid-infrared (mid-IR) exhibit quality factors (lifetime multiplied by frequency) of several hundred, while TMD excitons in the visible range can have line widths of microelectronvolts.
- Strong Field Enhancement. When polaritons are excited by external illumination, their associated electric field can be enhanced by several orders of magnitude relative to the incident light.
- Strong Optoelectronic Response. Materials like graphene and TMDs can undergo a dramatic change in the optical response under electrical doping (e.g., via gating), which can switch polaritons on and off or shift them beyond their line width. For instance, carrier density modulation in graphene can shift plasmon resonances by tens of percent, while gating in TMDs can strongly modify exciton oscillator strength and linewidth.
- High Susceptibility to External Perturbations. Thermal heating, mechanical stretching, magnetic fields, and interactions with additional neighboring materials can also induce substantial, unity-order changes in the linear and nonlinear optical responses of materials.
- Large Nonlinear Response. 2D materials exhibit remarkable intrinsic nonlinear responses, with graphene and TMDs featuring nonlinear susceptibilities that rival those of the best available nonlinear materials.

The extreme optical sensitivity and strong resonant behavior of 2D materials motivate their integration with photonic resonators, where optical fields can be further enhanced and controlled. One such resonant platform is guided mode resonance (GMR) structures, which provide a powerful route to enhance and tailor the optical response of dielectric materials such as WS_2.

While monolayer WS_2 exhibits unique excitonic and valley-dependent properties, the focus of this thesis is on bulk WS_2 layers with thicknesses of 70–80 nm. At these thicknesses, WS_2 provides a mechanically robust, high-index material that can be directly patterned into photonic nanostructures. This enables the realisation of guided-mode resonant devices that are compatible with standard nanofabrication processes and readily integrated with other substrates, optical fibers, and two-dimensional materials.

1.2 Guided Mode Resonance

Guided mode resonances (GMRs) occur in diffraction gratings composed of high-index materials that support leaky guided modes within the grating layer. When the phase-matching condition between the incident light and a guided mode is satisfied, sharp resonances appear in the reflection or transmission spectrum. These resonances typically exhibit quality factors ranging from tens to several hundreds, depending on grating geometry and material loss. In this work, GMRs are realised in bulk WS_2 layers with thicknesses of approximately 70–80 nm, which act as high-index waveguiding layers capable of supporting guided optical modes.

The grating parameters such as period, duty cycle, and thickness are designed so that the resonance wavelength is determined primarily by the grating periodicity and effective refractive index of the guided mode. GMRs are characterized by pronounced spectral features and by strong near-field enhancement, often exceeding one to two orders of magnitude relative to the incident field. The relatively large thickness of bulk WS_2 enables efficient mode confinement and provides sufficient optical path length for strong light–matter interaction within the resonant structure.

When thin layers of WS_2 are patterned in the region of maximum field enhancement of a GMR structure, the optical absorption and light–matter interaction can be significantly amplified. In contrast to monolayer WS_2, bulk WS_2 can be directly patterned using standard nanofabrication techniques such as electron-beam lithography and reactive ion etching, offering improved mechanical robustness and fabrication reliability. This makes bulk WS_2 particularly suitable for the realization of resonant photonic structures where the photonic response, rather than excitonic emission, is the primary focus.

As a result, GMRs find applications in a wide range of fields, including laser sensors, photodetectors, polarizers, spectrometers, and optical filters [7]. In addition, bulk WS_2 GMR structures can be transferred onto different substrates, integrated with optical fibers, or combined with other two-dimensional materials, providing a versatile platform for hybrid photonic devices and scalable resonant systems.

1.3 Thesis Outline

Chapter 2 introduces Maxwell's equations and explains how they describe light and its interaction with dielectric materials. The concepts of guided modes and diffraction are then presented, after which these principles are combined to explain GMRs and their key properties.

Chapter 3 discusses the simulation methods and computational tools used throughout this work. The simulation results are presented and their role in guiding the initial design and optimisation process is explained.

Chapter 4 details the fabrication of GMR gratings using electron-beam lithography and reactive ion etching in thin layers of WS_2. The resulting grating geometries are

verified using scanning electron microscopy, and the optical resonances are characterised through measurements of the reflection spectra.

Chapter 5 presents and discusses the experimental results, including a comparison with the simulations to evaluate the accuracy and limitations of the models.

Chapter 6 concludes the thesis by summarising the main findings and outlining potential directions for future research. Possible extensions of the work into 2D nano structures and avenues for further development are also discussed.

Chapter 2

Theoretical background

2.1 Maxwell's Equations and Photonics Crystals

Maxwell equations are the foundation of electromagnetic theory. Maxwell's equations describe how electric and magnetic fields behave in materials. These equations are given in the form of

$$\nabla \cdot \mathbf{E} = \frac{\rho}{\epsilon} \tag{2.1}$$

$$\nabla \cdot \mathbf{B} = 0 \tag{2.2}$$

$$\nabla \times \mathbf{E} = -\frac{\partial \mathbf{B}}{\partial t} \tag{2.3}$$

$$\nabla \times \mathbf{B} = \mu \mathbf{J} + \mu\epsilon \frac{\partial \mathbf{E}}{\partial t} \tag{2.4}$$

Equations 2.1 to 2.4 are the derivative form of Maxwell equations. They were given by Maxwell as complete solution to Gauss and Ampère's law. Using these equation we can get interesting results, describing electric and magnetic property of materials or system.

The symbols used in Maxwell's equations represent fundamental electromagnetic quantities: **E** denotes the electric field, which describes the force acting on a unit positive charge; **D** is the electric displacement field, accounting for the influence of material polarization in response to the electric field; **B** represents the magnetic flux density, indicating the strength and direction of the magnetic field; **H** is the magnetic field intensity, associated with magnetic effects produced by currents and independent of material magnetization; ρ is the electric charge density, expressing the amount of charge per unit volume; **J** denotes the electric current density, describing the flow of charge per unit area; ϵ is the electric permittivity of the medium, characterizing how the material responds to

an electric field; μ is the magnetic permeability, indicating the material's response to a magnetic field; $\mathbf{C}$ represents the speed of light in vacuum, which relates electric and magnetic fields in wave propagation; and ω is the angular frequency, defining the rate of oscillation of time-harmonic electromagnetic fields.

Other form of Maxwell's Equations is Gaussian which are described in the form of D and H.

$$\nabla \cdot \mathbf{D} = \mathbf{4}\pi\rho \tag{2.5}$$

$$\nabla \cdot \mathbf{B} \ = 0 \tag{2.6}$$

$$\nabla \times \mathbf{E} = -\frac{1}{\mathbf{C}}\frac{\partial \mathbf{B}}{\partial t} \tag{2.7}$$

$$\nabla \times \mathbf{H} = \frac{1}{\mathbf{C}}\frac{\partial \mathbf{D}}{\partial t} + \frac{4\pi}{C}\mathbf{J} \tag{2.8}$$

The component of D and E are related to one other through the following relation [8][9]

$$\mathbf{D}_i = \sum_i \epsilon_{ij}\mathbf{E}_{ij} + \sum_j \kappa\chi_{ijk}\mathbf{E}_j\mathbf{E}_k + 0(\mathbf{E})^3 \tag{2.9}$$

Several assumptions are made[8]. The first assumption is that the field strengths are small so that only the linear terms in equation 2.9 contribute. The second assumption is that the dielectric material is macroscopic and isotropic, so that $\mathbf{E}$ and $\mathbf{D}$ are then related by a scalar dielectric constant $\epsilon(r)$. The third assumption is that the dielectric constant is independent of frequency. The fourth assumption is that only low-loss dielectrics are considered so that $\epsilon(r)$ can be assumed to be real. With this assumptions the relation between $\mathbf{E}$ and $\mathbf{D}$ is as followed[9]:

$$\mathbf{D} = \epsilon(r)\mathbf{E} \tag{2.10}$$

$\mathbf{B}$ and $\mathbf{H}$ are related to each other through constitutive relation as follows,

$$\mathbf{B} = \mu\mathbf{H} \tag{2.11}$$

For most dielectric materials of practical interest [8] the magnetic permeability μ is equal to unity. It is therefore assumed that the following relation between $\mathbf{B}$ and $\mathbf{H}$ holds

$$\mathbf{B} = \mathbf{H} \tag{2.12}$$

It is further assumed that there is no free electric charge ρ or current $\mathbf{J}$, Maxwell's equations reduced to

$$\nabla \cdot \mathbf{D} = 0 \tag{2.13}$$

$$\nabla \cdot \mathbf{B} = 0 \tag{2.14}$$

$$\nabla \times \mathbf{E} = -\frac{1}{c}\frac{\partial D}{\partial t} \tag{2.15}$$

$$\nabla \times \mathbf{H} = \frac{1}{c}\frac{\partial D}{\partial t} \tag{2.16}$$

For the study of the photonics, Maxwell's equations are simplified with assumption that there is no free electric charge ρ or current $\mathbf{J}$

With this assumption, using equation 2.10 and 2.16 we get

$$\nabla \times \mathbf{H} - \frac{1}{c}\frac{\partial \epsilon(r)\mathbf{E}}{\partial t} = 0 \tag{2.17}$$

Harmonics mode can be expressed in terms of complex exponentials,

$$\mathbf{H}(r,t) = \mathbf{H}(r)e^{i\omega t} \tag{2.18}$$

$$\mathbf{E}(r,t) = \mathbf{E}(r)e^{i\omega t} \tag{2.19}$$

Using equations 2.18 and 2.19 in equations 2.15 and 2.17 gives the resulting equations (see Appendix),

$$\nabla \times \mathbf{E}(r) + i\frac{\omega}{C}\mathbf{H}(r) = 0 \tag{2.20}$$

$$\nabla \times \mathbf{H}(r) - i\frac{\omega}{C}\epsilon(r)\mathbf{E}(r) = 0 \tag{2.21}$$

Dividing equation 2.21 with $\epsilon(r)$ both the side and then taking curl, and using equation 2.20 in to resultant equation, we can obtain (see Appendix),

$$\nabla \times \frac{1}{\epsilon(r)}\nabla \times \mathbf{H}(r) = (\frac{\omega}{C})^2\mathbf{H}(r) \tag{2.22}$$

Equation 2.22 also referred as **master equation for photonics crystals**. Magnetic field form of the equation typically used as it results in an ordinary eigenvalue problem. The left-Hand side of equation 2.22 can be treated as an operator Θ, operating on $\mathbf{H}(r)$. This simple change in notation makes the form of Maxwell's equation look like and eigenvalue problem[8]

$$\Theta\mathbf{H}(r) = (\frac{\omega}{C})^2\mathbf{H}(r) \tag{2.23}$$

The electric field form of the equation can be derived as well; however, solution to the resultant generalised eigenvalue problem is much more difficult to solve numerically[8]

2.1.1 Scaling Properties of Maxwell's Equations

One interesting feature of electromagnetism in dielectric media is that there is no fundamental length scale other than the assumption that the system is macroscopic. In atomic physics, the spatial scale if the potential function is generally set by the fundamental length scale of the Bohr radius. For photonic crystal there is no fundamental constant with the dimensions of length - the master equation (equation 2.22) is scale invariant. This leads to simple relationships between electromagnetic problems that differ only by a contraction or expansion of all distances. The solution of the problem at one length scale determines the solution at all other length scale [8]. This simple fact is of considerable practical importance.

Just as there is no fundamental length scale, there is also no fundamental value of the dielectric constant. Suppose we know that harmonics modes of the system with dielectric configuration $\epsilon(r)$, and we are curious about the modes of a system with dielectric configuration that differs by a constant factor everywhere, so that $\epsilon'(r) = \frac{\epsilon(r)}{s^2}$ substituting $s^2\epsilon'$ for ϵ in equation 2.22 gives,

$$\nabla \times (\frac{1}{\epsilon'(r)}\nabla \times \mathbf{H}(r)) = (\frac{s\omega}{C})^2\mathbf{H}(r) \tag{2.24}$$

The harmonic modes $\mathbf{H}(r)$ of the new system are unchanged,; however, the relation between $\mathbf{E}$ and $\mathbf{H}$ has changed by the factor of s. The frequencies are all scaled by factor s. If we multiply the dielectric constant everywhere by a factor of $\frac{1}{4}$, the mode patterns are unchanged but their frequencies double.

With the above two relations, we see that if we scale ϵ by s^2 and also rescale the coordinates by s, the frequency ω is unchanged. This simple scaling invariance is a special case of more general coordinate transformations. It turns out that any coordinate transformation can be replaced simply by a change of ϵ and μ while keeping ω fixed[10].

2.2 Total Internal Reflection and Slab Waveguide

In this section we will try to keep discussion in terms of classical physics keeping it in simple language. However it has great importance for understanding more complex topics. In later we will try to connect over discussion to more relevant topic of guided mode in 1D grating, one type of photonics crystal structures.

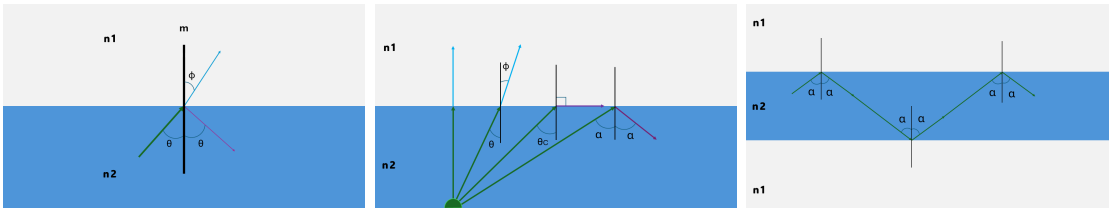

(a) (b) (c)

Figure 2.1: Ray passing from dense material to light material ($n_2 > n_1$). Total internal reflection at α. Classical way of understanding guided way by the different reflective index materials.

The reflraction of light ray at an interface between two dielectrics ϵ_1 and ϵ_2, illustrated in figure 2.1b is usually described in terms of Snell's law. Relation between reflective index and dielectric constant of medium for this peruse is given by $\epsilon_i \approx n^2$. **Snell's law** is given by

$$n_1 \sin(\theta) = n_2 \sin(\phi) \tag{2.25}$$

or more tredisnaly $n_1 \sin(\theta_1) = n_2 \sin(\theta_2)$, where θ_1 is angle made by ray to the normal in medium of n_1 reflective index and θ_2 is angle between ray and normal in medium of n_2 reflective index.

$$\theta = \sin^{-1}(\frac{n_2}{n_1}) \cdot \phi \tag{2.26}$$

If $\theta > \sin^{-1}(\frac{n_2}{n_1})$ then it is necessary that $\sin(\phi) > 1$ which is not possible, result of this that ray is totally reflected. For the maximum value of $\sin(\phi) = 1$ for which $\phi = 90°$, θ is called **critical angle** θ_c. The critical angle $\theta = \sin^{-1}(\frac{n_2}{n_1})$ exists only for $n_2 < n_1$, so total internal reflection occurs only within the higher-index medium. Snell's law, however, is simply the combination of two conservation laws that follow from symmetry: conservation of frequency ω(from the linearity and time invariance of the Maxwell equations), and conservation of the component $k_{||}$ of the k that is parallel to the interface. In particular, $k_{||} = |k| \sin(\theta)$ and $|k| = \frac{n\omega}{C}$ from the dispersion relation. We obtain Snell's law by setting $k_{||}$ equal on both sides of the interface. The advantage of thinking this way about the problem is that we are now in the a position to generalize beyond the ray optics.

Optical fibers and optical waveguides consist of a core, in which light is confined, and a cladding, or substrate surrounding the core, as shown in Fig. 2.2. The reflective

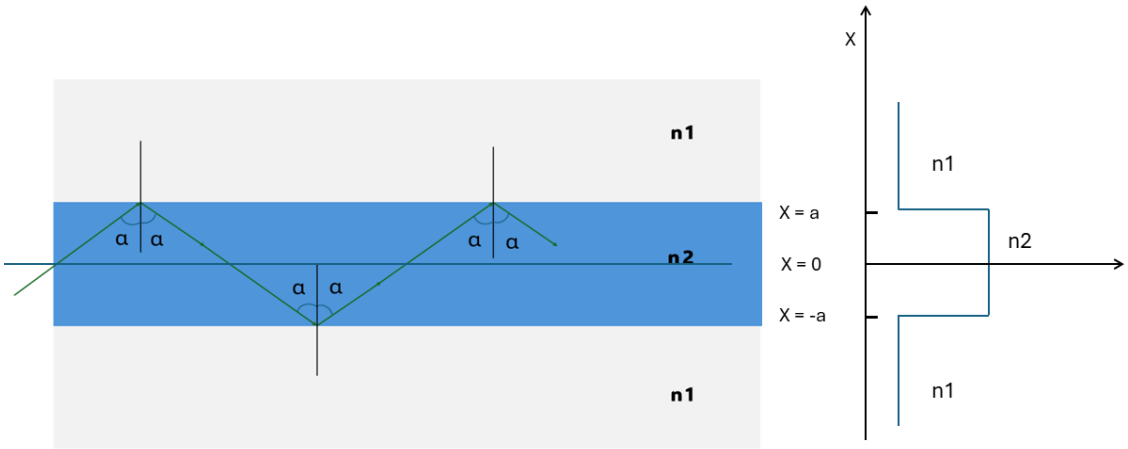

Figure 2.2: Basic structure and reflective-index profile of the optical waveguide. $n_2 > n_1$.

index of core n_2 is higher then that of the cladding n_1. There fore the light beam that is coupled to the end face of the waveguide is confined in the core by total internal reflection. The condition for total internal reflection at the core-cladding interface is given by $n_2 \sin(\pi/2 - \phi) \geq n_1$. Since the angle ϕ is related with the incident angle θ by $\sin(\theta) = n_2 \sin(\phi) \leq \sqrt{n_2^2 - n_1^2}$, we obtain the critical condition for the total internal reflection as

$$\theta \leq \sin^{-1} \sqrt{n_2^2 - n_1^2} = \theta_{max} \tag{2.27}$$

The refractive index difference between core and cladding is of the order of $n_2 - n_1 = 0.001$. Then θ_{max} in equation 2.27 can be approximated by

$$\theta_{max} \approx \sqrt{n_2^2 - n_1^2} \tag{2.28}$$

θ_{max} denotes the maximum light acceptance angle of the waveguide and is known as the numerical aperture(NA)[11].

The relative refractive-index difference between n_2 and n_0 is defined as

$$\Delta = \frac{n_2^2 - n_1^2}{2n_2^2} \cong \frac{n_2 - n_1}{n_2} \tag{2.29}$$

Δ is commonly expressed as a percentage. The numerical aperture (NA) is related to the relative- index difference Δ by

$$NA = \theta_{max} \cong n_1\sqrt{2\Delta} \tag{2.30}$$

2.3 Evanescent Wave

The transmitted wave is described by $\mathbf{k_2}$, whose z-component is

$$k_{2,z} = n_2 k_0 \cos(\theta_2) \tag{2.31}$$

The cos-term can be written as

$$\cos(\theta_2) = \pm\sqrt{1 - \sin^2(\theta_2)} = \pm\sqrt{1 - \left(\frac{n_1}{n_2}\sin(\theta_1)\right)^2} \tag{2.32}$$

Where Snell's law (Eq.2.25) was applied. When $\theta_1 > \theta_c$ the term inside the square root is negative, which leads t a purely complex z-component of k_2.

k_0 in Eq.2.31 is described as vacuum wave number and it is related to wavelength of wave or (incident wave) λ_0 as,

$$\lambda_0 = \frac{2\pi}{k_0} \tag{2.33}$$

λ_0 is wavelength of wave described by wave equation

$$\left(\nabla^2 - \epsilon\mu_0\frac{\partial^2}{\partial t^2}\right)E = 0 \tag{2.34}$$

Equation 2.34 is decoupled wave equation, given from Guass's law (Eq.2.1) and Amperes's law (Eq. 2.4). Solution of this wave equation is given by a plane wave ,

$$E(r,t) = E_0 \exp^{i(k_n \cdot r - \omega t)} \tag{2.35}$$

Whose propagration direction is along the wave vector k_n, ω is the angular frequency. In three-dimensional space, a wavefront is defined as the surface corresponding to a constant arbitrary phase $\phi = (k_n \cdot r - \omega t) = \phi_0$. The wavefronts propagate at a phase velocity

$$v = \frac{\omega}{k_n} = \frac{1}{\sqrt{\epsilon\mu_0}} = \frac{C}{n} \tag{2.36}$$

which corresponds to the speed of light in vacuum $C = \frac{1}{\sqrt{\epsilon\mu_0}}$, divided by the refractive index $n = \sqrt{\epsilon_r}$. In vacuum, the refractive index is $n = 1$.

When plugging Eq 2.31 and 2.32 into the plane wave equation (2.34), it is found that the wave in the low index medium is described by an exponentially decaying amplitude along the z-axis,

$$k_2(z) \propto \exp^{-kz} \tag{2.37}$$

with

$$k = k_0\sqrt{n_1^2 \sin^2(\theta_1) - n_2^2} \tag{2.38}$$

Note that the solution of Eq 2.32 of the opposite sign corresponds to an exponentially increasing solution and is discarded, as it is not physical.

Th evanescent wave can be characterised by its penetration depth $l = \frac{1}{k}$ corresponding to the distance at which the amplitude drops by a factor of $\frac{1}{\exp}$. The depth l decreases when θ_1 or n_1 are increased, or when n_2 is decreased.

2.4 Guided Mode

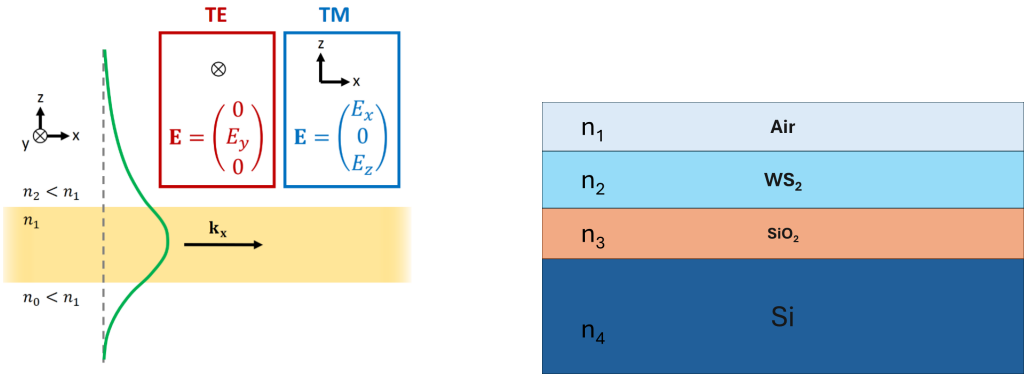

Figure 2.3: Single layer slab waveguide, reproduced from [1]. Schematic of a slab waveguide with intensity profile of the fundamental guided mode (green) propagating along the x-axis. The oscillation direction of the electric field for the TE and TM polarisation is shown in the red and blue frame, respectively(left). Multilayered slab waveguide illustration(right) with values of $n_1 = 1$, $n_2 = 5.04$, $n_3 = 1.46$, $n_4 = 3.85$ at $\lambda = 650nm$

A slab waveguide is a structure that is able to confine light in one arbitrary dimension z, allowing propagation along the orthogonal directions x and y, see Fig 2.3.

With dielectric materials, the light confinement can be achieved with TIR. In order for TIR to occur in the positive and negative z-direction, the refractive index of the slab n_s must be greater than the indices n_a and n_b of the medium above and below the slab, respectively.

In the xy-plane, the indices are assumed infinite and homogeneous. Consider propagation along the arbitrary x-axis, which makes the solution independent of y. This leads to a solution with an envelope in z, propagating in plane as

$$E(x,z) = E(z)\exp^{i(k_x x - \omega t)} \tag{2.39}$$

where the in-plane wave vector component is $k_x = n_{eff}k_0$, with effective refractive index n_{eff}. The envelope along the z-axis is described by

$$\left(\frac{\partial^2}{\partial z^2} - k_x^2\right) E(z) = 0 \tag{2.40}$$

with

$$k_z^2 = k_n^2 - k_x^2 \tag{2.41}$$

Note that $k_n = nk_0$ depends on the medium index n, which leads to three different solutions for the envelope in the three layers.

For guided modes, the envelope is described by evanescent tails in the surrounding media, and a sinusoidal wave inside the slab. At the interfaces, the wave must satisfy boundary conditions that depend on the polarisation of the mode, see the next section (2.5).

For a given wavelength λ_0, one or more solutions of Eq 2.40 are possible, corresponding to different effective indices. The effective index n_{eff} of the guided mode is given by a weighted sum of the material indices, where the weights are determined by the envelope. The order of the guided mode is given by the number of nodes of the sinusoidal wave inside the slab, where a higher order mode corresponds to a lower n_{eff} .

2.5 Boundary Conditions

For transverse electric (TE) modes, the electric field is orthogonal to the propagation direction and the index interfaces. If the confinement is along z and propagation along x, the only non-zero electric field component is E_y (Fig 2.3).

The other polarisation of interest is transverse magnetic (TM), where it is the magnetic field whose oscillation is orthogonal to the propagation direction and the interfaces. In this case, the non-zero electric field components are E_x and E_z. Note that there is an electric field component along the propagation direction of the mode, which would not be possible for plane waves in free space.

Gauss' law (Eq 2.1) implies that the displacement field component $D_z = \epsilon E_z$ normal to the interface is continuous. With Faraday's law (Eq 2.3), it can be shown that the

tangential components of the electric field E_x and E_y are continuous.

As the TE and TM modes satisfy different boundary conditions, they have different envelopes along z. Therefore, they have a different effective indices n_{eff} and different field distributions for a given λ_0.

2.6 Thin Film Interference

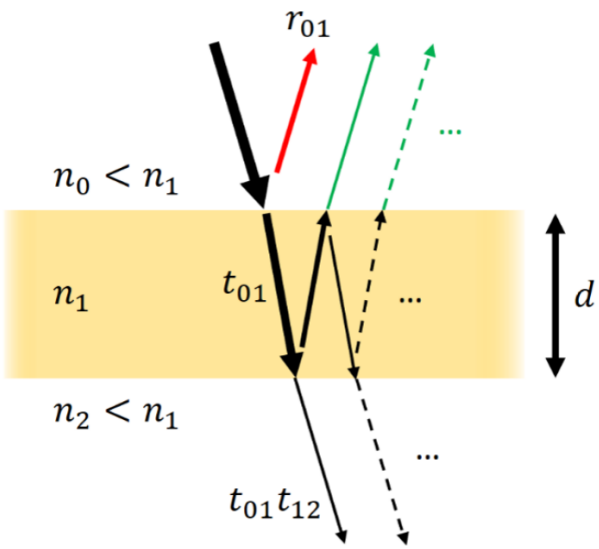

Figure 2.4: Thin film interference of index n_1 with incoming ray(black) and showing its component.

As described in the previous section, a thin film of high index material surrounded by lower index media can support guided modes. The light in such modes is confined to the slab, i.e. it cannot couple to out-of-plane propagating waves. This implies that the inverse is not possible either: A beam of light propagating in free space that impinges on the slab out-of-plane cannot couple to the guided modes either.

Instead, the beam will be partially reflected and transmitted at the first index interface with amplitude coefficients r_{01} and t_{01}, respectively, see Fig 2.4. Note that the reflected beam (red arrow) experiences a phase change of π, as $n_1 > n_0$. The transmitted part propagates on to the second index interface, where it is partially reflected, travels back up to the first interface and is partially transmitted (green, solid arrow). The reflected part keeps travelling between the interfaces, with its amplitude decreasing with each round trip, as it is partially transmitted (green, dashed arrow) at each interface.

It can be shown, using geometry arguments and Snell's law, that the phase difference accumulated during one round trip inside the slab is given by,

$$\Delta\phi = 2n_1 k_0 d\cos(\theta_1) \tag{2.42}$$

where $k_0 = \frac{2\pi}{\lambda_0}$, d is the film thickness, and θ_1 is the angle of the refracted beam inside the slab.

The resulting reflection spectrum represents the sum of all the individual portions of light from each round trip. Consider a fixed angle of incidence. If the wavelength is such that $\Delta\phi$ is a multiple of 2π, then all portions transmitted from within the thin film back into the medium of incidence constructively interfere with each other. The initial reflection of the incident beam (red arrow) has a π-shift with respect the sum of waves from inside the slab (green arrows), i.e. they destructively interfere. This corresponds to a dip in the reflection spectrum, or a peak in the transmission spectrum.

In contrast, if the phase difference is $\Delta\phi = \pi + m2\pi$ with $m \in Z$, the waves from consecutive round trips interfere destructively with each other, but the initial reflection is in phase with the portion of light coming back from the first round trip. This scenario corresponds to a peak in reflection.

Since the reflection coefficients of refractive index interfaces are generally low, peaks and dips in the spectrum are wide and slowly varying with λ_0. Note that the shape of the spectrum is slightly different for light whose electric field is oriented orthogonally to the plane of the incident and reflected beam (s-polarised) and light polarised parallel to the plane (p-polarised). This is due to the polarisation dependence of the reflection and transmission coefficients of the interfaces.

2.7 Diffraction Grating

Diffraction is one of the key phenomena that give rise to guided mode resonance, as it provides the coupling between guided modes and out-of-plane propagating waves (see next section).

Recall from section on Total Internal Reflection that a plane wave incident on a planar refractive index interface is partially reflected and propagates as a plane wave at a single, well defined angle. However, if the wave interacts with an object of a finite size comparable to the wavelength λ_0, it may be scattered into a continuous range of angles. In order to generate such scattering in a controlled manner, an optical diffraction grating may be created by periodically arranging multiple unit cells, each containing the same scattering object, with a period a of the order of λ_0. Fig 2.5 A) shows a grating with a plane wave at normal incidence.

Consider two neighbouring unit cells separated by the period a, as shown in Fig 2.5 B). The unit cell of the grating is approximated as a point source scattering a spherical wave into the surrounding medium of refractive index n. When two wave fronts meet in phase, they constructively interfere. If the path difference between the two waves is zero, their interference is always constructive. This case corresponds to diffraction order $m = 0$, with a diffraction angle that is equal to the angle of incidence flipped around the normal of the grating.

Constructive interference may also occur when a number m of wave fronts is "skipped"

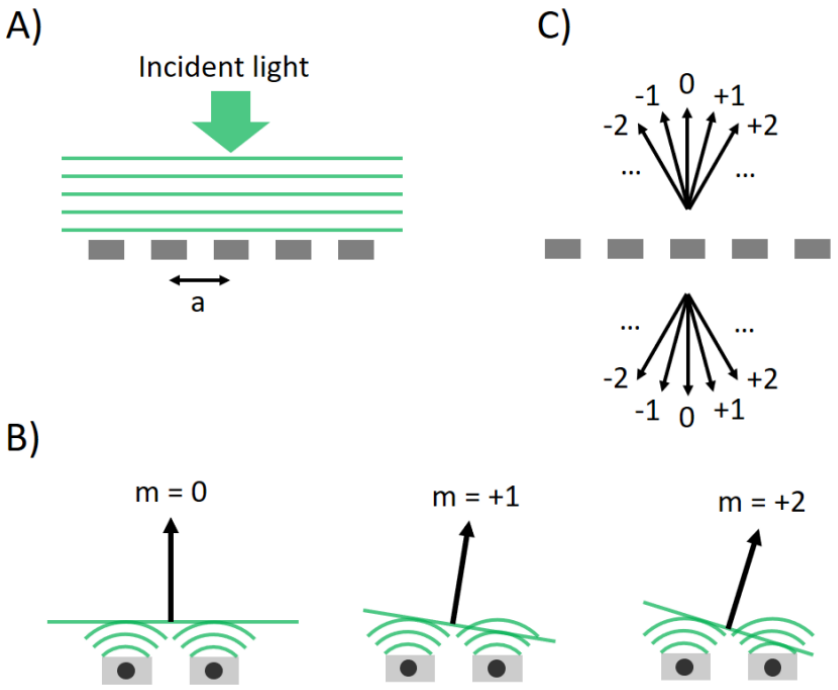

Figure 2.5: Schematic of an optical diffraction grating. A) Plane wave at normal incidence on the grating of period a. Wavefronts are represented by green lines. B) Two neighbouring unit cells of the grating represented as point sources (black dots). The diffraction order m and corresponding propagation directions (black arrows) at angles for which the two waves interfere constructively. Green line: Diffracted wave front. C) Positive and negative diffraction orders in reflection and transmission.

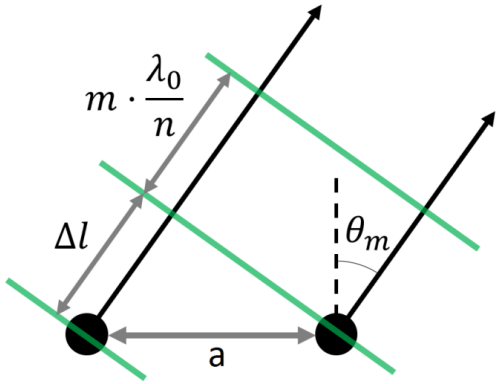

Figure 2.6: Schematic for the calculation of diffraction angles, with grating period a. For constructive interference at different angles θ_m, the path difference Δl is equal to m times the wavelength in medium $\lambda_n = \frac{\lambda_0}{n}$

between the two waves, e.g. $m = 1$ or $m = 2$ illustrated in Fig 2.5 B), which results in waves propagating at an angle. A finite number of diffraction orders may exist on both sides of the grating, see Fig 2.5 C). Note that half-way between two consecutive diffraction orders, the interference is destructive, i.e. no light can propagate along the corresponding direction

The diffraction angles are calculated for an incoming wave at normal incidence, using the schematic in Fig 2.6. For an observation point at angle θ and distance $d > a$ far away from the grating, the path difference between the two waves is given by

$$\Delta l = a \sin(\theta) \tag{2.43}$$

corresponding to a phase difference of

$$\Delta\phi(\theta) = kn\Delta l = \frac{n2\pi}{\lambda_0} a \sin(\theta) \tag{2.44}$$

Constructive interference occurs when $\Delta\phi = m2\pi$, with the integer m corresponding to the order of diffraction, which yields the diffraction angle

$$\theta_m = \sin^{-1}(m \cdot \frac{\lambda_0}{an}) \tag{2.45}$$

As the domain of the $\sin^{-1}$ function is [-1,1], the equation only allows real solutions when

$$|m| \leq \frac{an}{\lambda_0} \tag{2.46}$$

This means that for a given wavelength λ_0, a sufficient increase of the period a leads to an increase in the number of diffraction orders and reduces their angular spacing. On the other hand, if a is reduced so that

$$a < \frac{\lambda_0}{n} \tag{2.47}$$

the number of diffraction orders is only one, with order $m = 0$. It is important to notice that for a higher index medium, a larger number of diffraction orders might be available.

The key point to note is that the index n_g grating material has to be significantly higher than its surrounding media, so that the resulting effective index n_{eff} satisfies

$$n_{eff} > n_s \tag{2.48}$$

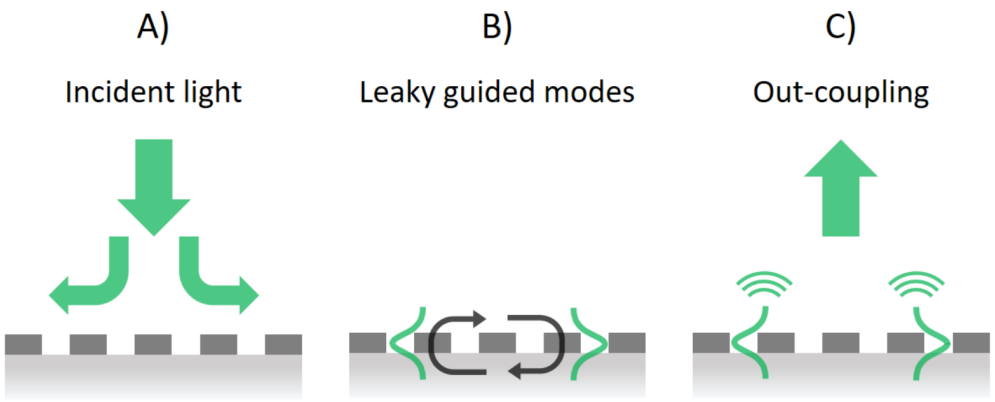

Figure 2.7: Basic principles involved in a GMR. A) A beam of light at normal incidence, diffracting into the grating layer. B) Guided modes (green profiles) experiencing in-plane diffraction (black arrows). C) The guided modes are leaky and couple to out-of-plane free space radiation.

and

$$n_{eff} > n_m \tag{2.49}$$

for the grating layer to be able to support guided modes.

For a given wavelength λ_0, the period a is designed small enough, so that in the medium and substrate, only the 0^{th} order of diffraction is supported (Eq 2.47). However, a is chosen big enough for the first diffraction orders $m = \pm 1$ to exist in the grating layer, i.e.

$$\frac{\lambda_0}{n_{eff}} \leq a \leq \frac{\lambda_0}{n_i}, \quad i \in \{substrate, medium\} \tag{2.50}$$

When a beam of light with wavelength λ_0 impinges at normal incidence on the grating (Fig 2.7 A), the zero order light only experiences the thin film response of the grating. The first order light is diffracted into the grating layer and couples to a leaky guided mode.

As the mode propagates along the grating (Fig 2.7 B), a small amount of light is scattered at each interface between the grating ridge and the gap. As a result, the leaky guided mode experiences two kinds of diffraction. On one hand, in-plane diffraction causes the light to bounce back and forth (black arrows) along the direction of periodicity. On the other hand, out-of-plane diffraction (Fig 2.7 C) allows the light to couple back out to free space radiation - the inverse process of A).

If λ_0 and a are such that all the scattered waves are in phase, the resonance condition is met. This phase-matching condition relates the effective index n_{eff} of the leaky guide mode to the resonant wavelength λ_{res} and the grating period a as

$$n_{eff} = \frac{\lambda_{res}}{a} \tag{2.51}$$

In this case, the total out-coupled wave interferes with the light that experienced the thin film response at the start. Depending on whether the interference is constructive or destructive, the incident wave may be completely reflected or transmitted.

2.8 Bloch Modes

Consider a periodic permittivity

$$\epsilon(x) = \epsilon(x + a) \tag{2.52}$$

with period a, choosing the x-axis as the arbitrary grating direction.

According to Bloch's theorem [12], the solution to the wave equation (Eq 2.34) in such a medium is given by

$$E_{kx}(x) = \exp^{ik_x x}\, uk_x(x) \tag{2.53}$$

which corresponds to a plane wave $\exp^{ik_x x}$ modulated by a function $u_{kx}(x)$that has the same periodicity as $\epsilon(x)$.

Therefore, the wave can be expressed as

$$E_{kx}(x) = \sum_{m=-\infty}^{\infty} E_m \exp^{i(k_x + mG_x)x}, m \in \mathbb{Z} \tag{2.54}$$

with the reciprocal lattice vector $\mathbf{G}$, whose only non-zero component in this example is

$$G_x = \frac{2\pi}{a} \tag{2.55}$$

The Bloch modes can therefore be viewed as a linear combination of a discrete set of plane waves with different in-plane wave vector components. For example, in the case of the GMR mode, light at normal incidence with $k_x = 0$ can couple to guided waves $k_x = \pm G$, since they are part of the same Bloch mode.

2.9 Photonic Band Gap

The photonic band gap is well illustrated by the modes on either side of the first band gap at $k_x = \frac{G_x}{2}$. According to Eq 2.54, this mode has plane wave components

$$E_0 \exp^{i\frac{G_x}{2}x} \tag{2.56}$$

and

$$E_{-1} \exp^{-i\frac{G_x}{2}x} \tag{2.57}$$

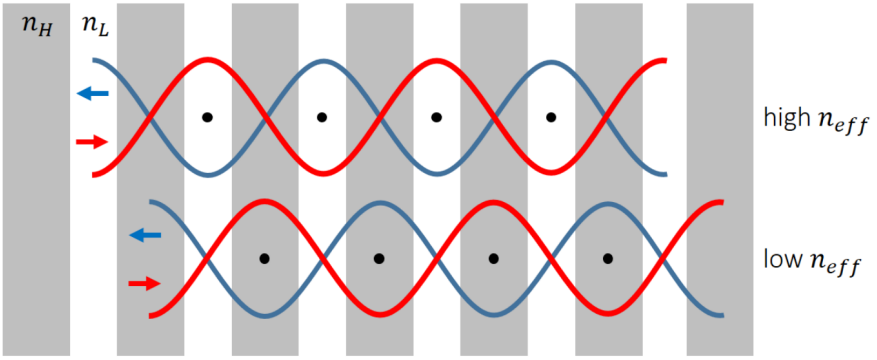

Figure 2.8: Illustration of counter-propagating waves in a GMR-grating, consisting of alternating sections of high (n_H) and low (n_L) refractive index. Counter-propagating waves in red and blue form a standing wave with nodes (black dots), where the waves cancel each other out. Between the nodes, the standing wave amplitude oscillates. The effective index depends on the position of the nodes and peaks of the standing wave.

As illustrated in Fig 2.8, the two waves have an in-plane wave vector of equal amplitude and opposite sign, i.e. they are two counter-propagating waves that form a standing wave. The nodes of the standing wave can either be located in the grating ridge or in the gap, in order to respect the symmetry of the system.

If the nodes are located in the gap, a large amount of the standing wave will overlap with the ridge, resulting in a higher effective index. If on the other hand the nodes are in the ridge, the wave will mainly overlap with the gap, resulting in a lower refractive index.

Between the lower and higher effective indices, no solution is available, i.e. no Bloch mode exists in the grating layer. This corresponds to the photonic band gap. A beam of light hitting the grating at a forbidden wavelength lying within a gap, will simply experience the thin film response of the grating layer.

2.10 Photonic Band Structure

In the equation for the Bloch mode (Eq 2.54), it can be seen that $E_{kx+lG}(x) = E_{kx}(x)$,for any $l \in \mathbb{Z}$. This shows that all the information provided by the equation can be folded back into a finite range of k_x, e.g. $-\frac{G_x}{2} \leq k_x \leq \frac{G_x}{2}$, which is the first Brillouin zone (FBZ). Due to the folding, a band structure is obtained, where different bands have different effective indices and corresponding resonant wavelengths for a given period.

The band diagram can be inferred from the resonant peaks in the optical reflection spectra at different incident angles. I simulate these spectra with the S4 software [13], which is an implementation of the semi-analytical rigorous coupled wave analysis (RCWA).

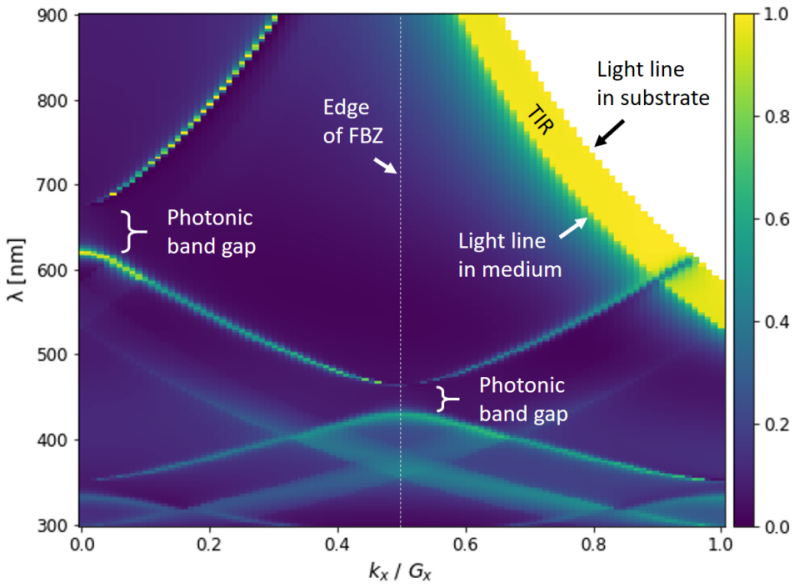

Figure 2.9: TE-polarised dispersion diagram of a GMR-grating, obtained by plotting the optical reflectance spectrum at different angles. Grating parameters: Period a = 400 nm, grating thickness t=150 nm, fill factor FF=0.75, grating material: SiN, substrate: glass, medium: water. Incidence from substrate side.

Consider, as an example, a silicon nitride grating on a glass substrate covered by a water medium. The refractive indices are assumed constant over the considered wavelength range, represented by the indices at $\lambda = 655$ nm of $n_g = 2.0368$, $n_s = 1.4693$ and $n_m = 1.333$ for the grating, substrate and medium, respectively. The corresponding band diagram (Fig 2.9) features distinct lines, which correspond to the photonic bands of the periodic structure. The values of k_x go beyond the FBZ, in order to illustrate the folding of the bands

The angle of incidence θ_x relates to the in-plane wave vector component as $k_x = k_n \sin(\theta_x)$. Only values of $k_x \leq k_n$ can be measured with this method, which corresponds to the light cone in the medium of index n. With incidence from the glass substrate side, a range of k_x is available in glass that can't propagate in the water medium. In this range, all the light will be reflected back into the glass eventually, which corresponds to TIR (section 2.2).

Note that here the y-axis is the wavelength λ, which means that lower band numbers are closer to the top in the figure. Several band gaps can be seen, e.g. at $\lambda \equiv 650$ nm between the second and third band at the Γ-point, i.e. where $k_x = 0$. A higher harmonic of this gap is found at approximately half the wavelength, $\lambda \equiv 350$ nm. The band gap at the edge of the FBZ at $\lambda \equiv 450$ nm is a higher harmonic of the lowest energy band gap, which was illustrated in the previous section. It is worth noticing that the wide TIR band folds back into the FBZ as well, but is not to be confused with the resonant modes.

In general, complete transmission and reflection is reached for resonances with incident angles inside the light cone, which only couple to in-plane waves that are outside the light cone. This regime corresponds to cases where only diffraction order zero exists inside the substrate and the medium, i.e. no light is lost to higher orders of diffraction, while the first diffraction orders $m = \pm 1$ within the grating layer match the resonant guided mode. Corresponding modes are found on either side of the first band gap at the Γ-point. They will be considered in more detail in the following section.

2.11 Q-factor and Resonance Wavelength

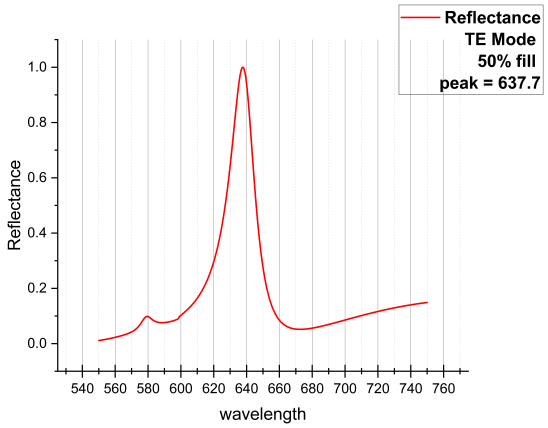

Figure 2.10: Simulation of 1D grating in Silicon Nitrate (SiN) with fill factor(FF) of 50%. $\lambda_{res} = 637.7$ nm. Structure consist Air - PMMA filled 1D grating in SiN - Fused Silica substrate.

A resonance peak can be characterised by its quality factor Q, which is defined as

$$Q = 2\pi \frac{U}{\Delta U} \tag{2.58}$$

with the energy U stored in the resonator and the energy ΔU dissipated per optical cycle.

Assume Q is a constant, and express ΔU in terms of the average temporal derivative of the energy

$$\Delta U = \frac{\dot{U}}{v_o} \tag{2.59}$$

which leads to the differential equation

$$\dot{U} = \frac{2\pi v_0}{Q} U \tag{2.60}$$

Which shows that in absence of a source, the energy inside the resonator decays exponentially

$$U(t) = U_0 \exp^{-\frac{t}{\tau}} \tag{2.61}$$

where U_0 is a constant and

$$\tau = \frac{Q}{2\pi v_0} \tag{2.62}$$

is the exponential energy decay time.

An electric field oscillating at v_0 and decaying in energy as Eq 2.61 can be expressed as

$$E(t) = E_0 \exp^{-\frac{t}{2\tau}} + i2\pi v_0 \tag{2.63}$$

Taking the Fourier transform of Eq 2.63 yields a Lorentzian line shape with a frequency half width at half maximum $\gamma = \frac{1}{2\pi}\frac{1}{2\tau}$, which allows to write the Q-factor as

$$Q = \frac{v_0}{2\gamma} \tag{2.64}$$

For narrow peaks in a wavelength spectrum, the Q-factor can be expressed in terms of the resonant wavlength $\lambda_0 = \frac{1}{v_0}$ and the full width at half maximum $\Delta\lambda = \frac{2\gamma}{\lambda^2}$, yielding

$$Q = \frac{\lambda_0}{\Delta\lambda} \tag{2.65}$$

Chapter 3

Simulation Method and Results

3.1 Simulation Tool

For the simulation of guided mode or photonics crystals S4 tool is used. **S4** (or simply S4) stands for Stanford Stratified Structure Solver, a frequency domain code to solve the linear Maxwell's equations in layered periodic structures. Internally, it uses Rigorous Coupled Wave Analysis (RCWA; also called the Fourier Modal Method (FMM)) and the S-matrix algorithm. The program is implemented using a Lua frontend, or alternatively, as a Python extension. S4 was developed by Victor Liu of the Fan Group in the Electrical Engineering Department of Stanford university [13].

There are a great variety of general-purpose tools available for computational electromagnetism (CEM), such as the finite difference time-domain (FDTD) method, finite-difference frequency-domain (FDFD) method, and the finite element method (FEM), that can be adapted to simulate three-dimensional structures with 2D periodicity. However, for the specific class of periodic structures composed of layers invariant in the direction normal to the periodicity, the Fourier modal method (FMM), also called rigorous coupled wave analysis (RCWA) or the scattering matrix method (SMM), is particularly suitable due to its Fourier basis representation. S^4 is an implementation of the FMM for computing modal expansions within layers, combined with a scattering matrix (S-matrix) algorithm to join together layers for solving electromagnetic fields throughout a three-dimensional structure[13].

The rigorous coupled-wave analysis (RCWA), or Fourier modal method (FMM), models electromagnetic fields in layered periodic structures by expanding them into eigenmodes with exponential dependence in the normal direction and Fourier components in the plane of periodicity. By enforcing field continuity at interfaces and combining layer scattering matrices, the method efficiently computes diffraction in complex multilayer gratings. Early RCWA work focused on sinusoidal gratings, later extending to 2D periodic structures with improved numerical stability. However, slow convergence—especially for metallic gratings under TM polarization—motivated major reformulations, most notably Li's Fourier factorization rules, which significantly enhanced accuracy. Subsequent fast Fourier factorization (FFF) methods further improved performance by introducing

local polarization bases. The S4 implementation incorporates all major stable formulations except adaptive spatial resolution (ASR), which, although powerful, complicates interface matching and may compromise accuracy. S4 thus remains a flexible, general, and extensible FMM platform suited for broad classes of periodic optical structures[13].

Due to its open source nature it gives us great flexibility in terms of use. It solves the frequency-domain Maxwell's equations using RCWA, which expands the electromagnetic fields and material permittivity in terms of spatial fourier harmonics. S4 represents the structures as a stack of periodic layers and computes how an incident electromagnetic wave couples to the allowed diffraction orders of the system. S4 employs the S-matrix algorithm to propagate electromagnetic modes through successive layers, which ensures numerical stability for highly multilayered structures. S4 allows users to define simulation geometries, like 1D gratings, 2D rectangles, circles, Ellipse, or even polygons; materials and excitation conditions through scripting. The solver outputs quantities such as reflection, transmission, absorption spectra, and field profiles, allowing us to investigate how structural parameters influence optical resonances. Combination of all of these qualities of S4 makes it a great and effective tool for designing and optimising photonic devices that rely on guided mode resonances.

3.2 Grating Geometry

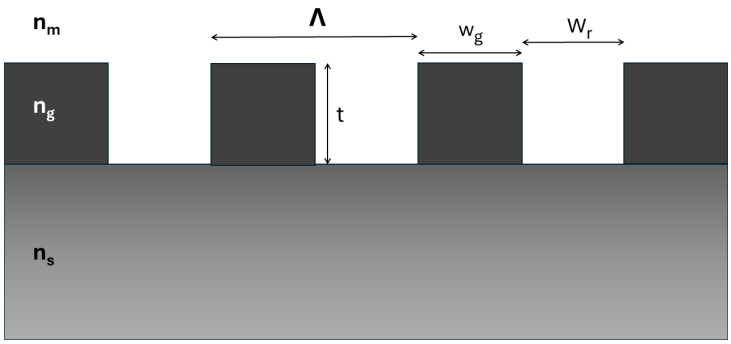

Figure 3.1: GMR-grating geometry, with grating thickness t, ridge width w_r, gap width w_g, period Λ, and refractive indices of the substrate (n_s), grating (n_g) and medium (n_m).

The geometry of a GMR-grating is parametrised according to Fig 3.1. The fill factor is defined as

$$FF = \frac{w_r}{\Lambda} \tag{3.1}$$

With the width w_r of the grating ridge and period Λ, it is also denoted by a

3.3 Simulation Results

Figure 3.2 illustrates the material configuration used in our simulations as well as the final device geometry. The structure consists of a silicon dioxide (SiO_2)on a silicon (Si) substrate, a tungsten disulphide (WS_2) guiding layer that forms the main grating material, and air as the top cladding. In Fig. 3.2 (left) the second layer is labelled as *Air*, this region can alternatively be replaced with other materials of different refractive indices, such as PMMA.

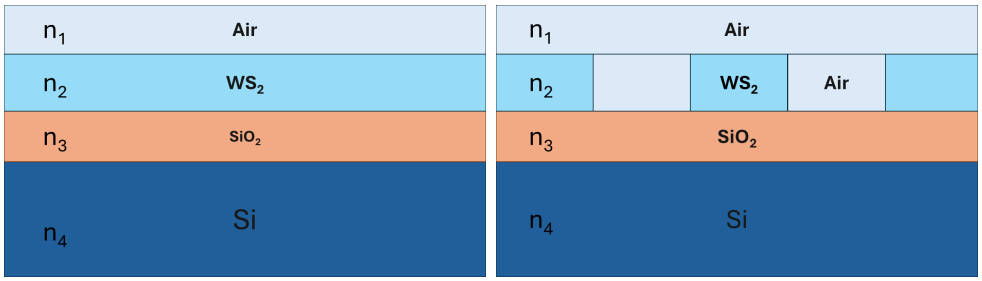

Figure 3.2: Slab waveguide illustration for simulation of 3.3. For all the simulations substrate Si was considered as infinite thickness similarly top layer of air with infinite thickness.

As an initial step, we simulated a simple one-dimensional slab waveguide. This provides a solid starting point for understanding the confinement behaviour of the WS_2 layer within the multilayer stack. For this initial model we considered only the real part of the refractive index and neglected material absorption. However, because WS_2 exhibits significant wavelength-dependent absorption, special care must be taken in selecting appropriate values for both the real index n and the extinction coefficient k, as shown in Fig. 6.1.

For the preliminary slab-waveguide simulation, we selected material parameters at a wavelength of 650 nm, since our goal is to design a structure capable of supporting guided modes at 650 nm and above. The refractive indices and layer thicknesses used were: $n_{air} = 1$; WS_2 only n is considered and it value is $n_{WS_2} = 5.3098$ and thickness is $t_{WS_2} = 75$nm as this is most common thickness we get from exfoliation 4.3; $n_{SiO_2} = 1.4565$ and thickness, t_{SiO_2} is 1000nm or 1 μm and finally for substrate we have used $n_{Si} = 3.6730$ nm.

The aim of selecting an optimal grating period and fill factor is to achieve a strong, well-defined TE resonance with a high Q-factor within the targeted wavelength range above 650 nm, while maintaining fabrication feasibility and robustness against process variations.

Fig. 3.3 shows the results of the simulation. This simulation was performed online using the tool "OMS: 1-D Mode Solver for Dielectric Multilayer Slab Waveguides" [14]. These results provide several important insights and serve as a valuable starting point for further analysis. Fig. 3.3a shows how the effective refractive index n_{eff} varies with wavelength, giving us an indication of where to expect guided modes and how the TE and TM modes are separated. From Fig. 3.3b we can estimate how the WS_2 layer thickness influences the mode profile.

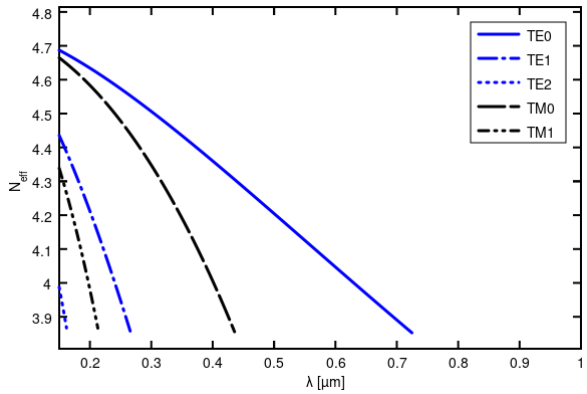

(a) a

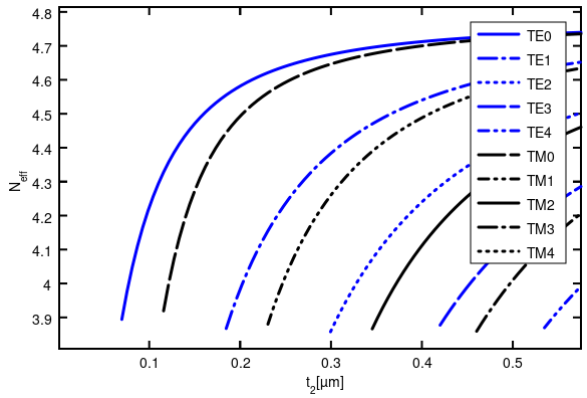

(b) b

Figure 3.3: Simulation of slab waveguide. a) N_{eff} vs wavelength (λ) for 75 nm thickness of WS_2 b) N_{eff} vs thickness of WS_2 material .

From the simulation, we obtain an effective index $n_{eff} = 4.24930$ for TE_0 mode at a wavelength of 650 nm. Using this value, we can estimate the required grating period by applying Eq. 2.51. Based on this equation, the calculated grating period (a or Λ) is 151 nm. Using this estimated period and considering the fill factor, we can perform additional simulations for various grating configurations to determine an optimal grating period.

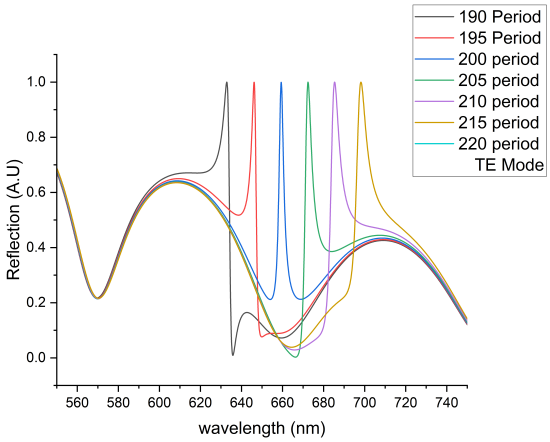

Figure 3.4: Simulation with various grating period from 190 nm to 220 nm with 80% fill factor(FF) for with WS_2 thickness of 75 nm

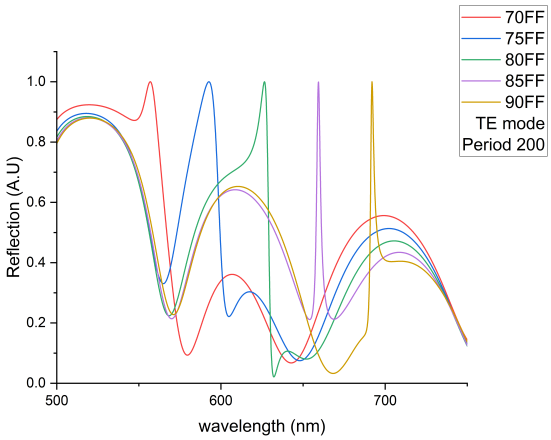

Figure 3.5: Simulation for various fill factor(FF) from 70% to 90% with the grating period of 200 nm and WS_2 thickness of 75 nm.

Considering all the results from slab waveguide we run the simulation for 80% fill factor to find the base period. From fig 3.4 we can see that good period were 200nm to 210 nm, with resonance wavelength $\lambda_{200} = 659.3$ nm; $\lambda_{205} = 672.4$ nm ; $\lambda_{210} = 684.9$ nm. as from previous results we know that thickens also affects final results, considering this we also ran the simulation to see this affects and expected outcome. we have run new simulation for finding batter matching fill factor and thickness combination. fig 3.5 and 3.6 shows results of various fill factor for the different thickness of 75nm and 80 nm. figure 3.7 shows results of various fill factor with period of 210nm. left is showing for TE mode and Right showing TM mode. from figure 3.7 we can see that TM mode is very broad mode. Figure 3.8 and 3.9 are showing Electric filed in the guided mode. figure 3.8

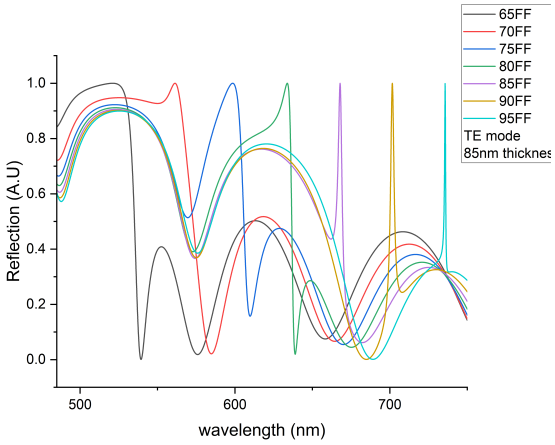

Figure 3.6: Simulation for various fill factor(FF) from 65% to 95% with the grating period of 200 nm and WS_2 thickness of 80 nm.

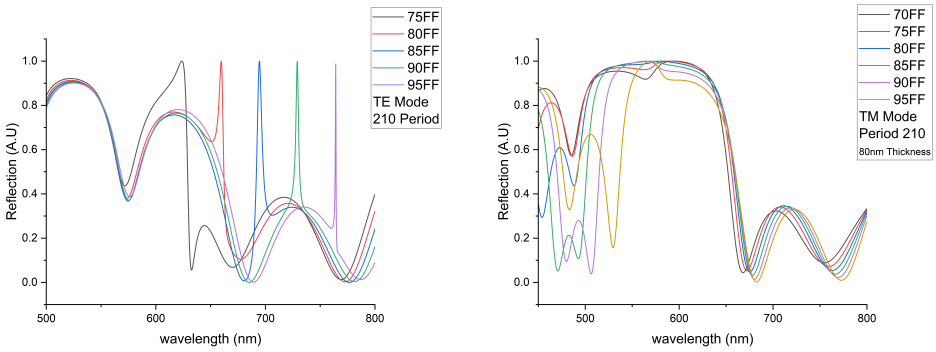

Figure 3.7: Simulation for various fill factor(FF) with the grating period of 210 nm and WS_2 thickness of 80 nm, left TE mode and Right TM mode.

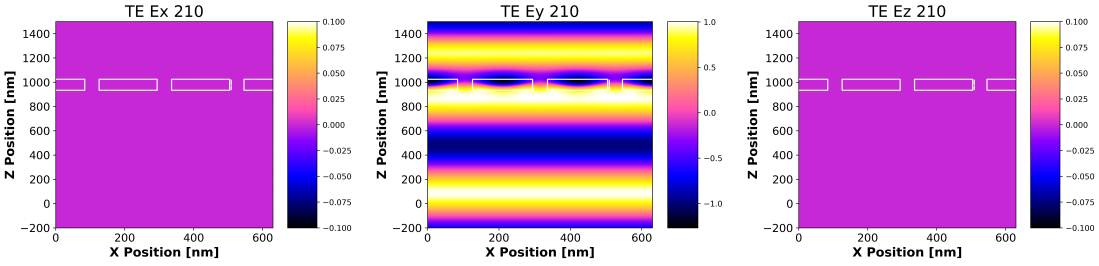

Figure 3.8: Electric filed distribution at wavelength of 660 nm in the WS_2 GMR structure shown in fig 3.2 with period of 210 nm and fill factor of 80% . TE mode for E_x , E_y, E_z, from left to right. E_x and E_z are zero.

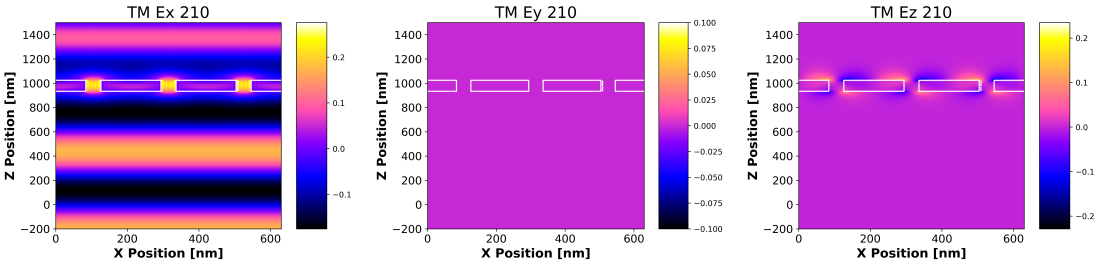

Figure 3.9: Electric filed distribution in GMR structure in WS_2 shown in fig 3.2 with period of 210 nm and fill factor of 80% . TM mode for E_x , E_y, E_z, from left to right. E_y is zero.

shows filed for TE mode and 3.9 shows filed for TM mode and we can say conclude that graph align very well with our theoretical part. From this results we have concluded that best starting point would be period of 200 with fill factor of 80% and thickness height close to 80nm. as we have to make few literation to this design based on experimental outcome.

From the simulation results figure 3.4,3.5,3.6,3.7, a clear and consistent trend is observed in both the resonance wavelength and the quality factor as a function of grating period and fill factor. Increasing the grating period leads to a systematic red-shift of the resonance wavelength for both TE and TM modes, which is expected from the phase-matching condition between the guided mode and the diffracted orders. Similarly, variations in fill factor significantly influence the effective refractive index of the grating region, resulting in shifts of the resonance wavelength and changes in the confinement strength of the guided modes. In general, higher fill factors increase the effective index of the grating, producing a red-shift in the resonance wavelength and, in certain configurations, an enhancement of the Q-factor due to improved mode confinement.

Chapter 4

Fabrication and Characterisation

4.1 Introduction

This chapter introduces the methods used for fabricating samples for experimental investigation. The fabrication process involves multiple stages. In the first step, suitable sample flakes are exfoliated. These flakes are then transferred onto a substrate. After transfer, the samples are coated for electron beam (E-beam) lithography (EBL). Following this, the samples undergo development and etching. Finally, measurements are carried out on the fabricated structures.Further details of each process are provided in their respective sections below.

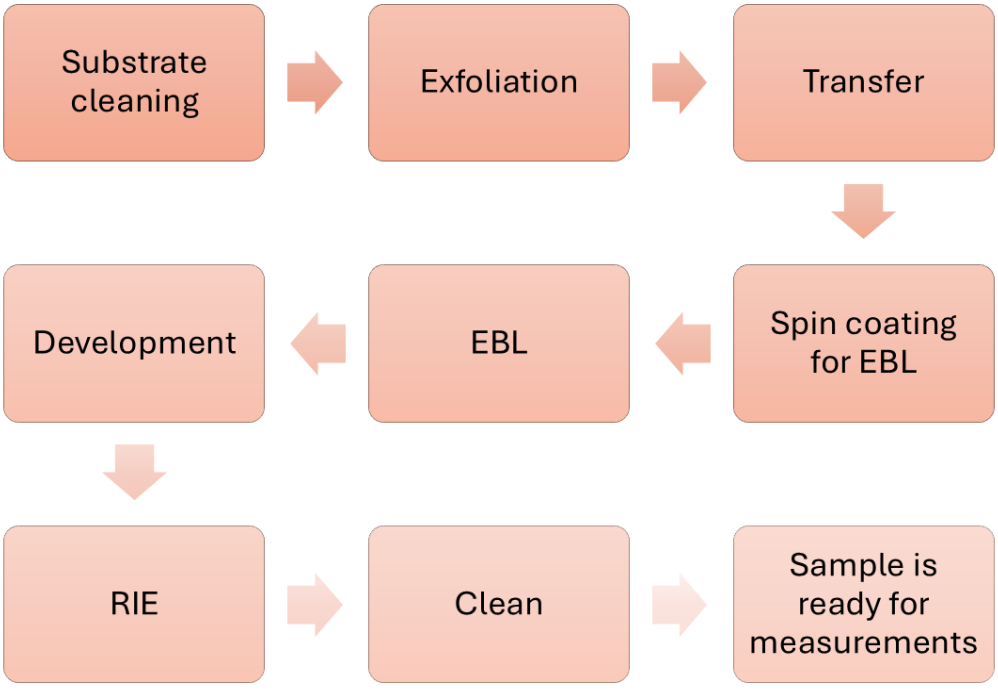

Figure 4.1: Work flow of fabrication process.

4.2 Cleaning

Different cleaning procedures were employed depending on the stage of fabrication. To prepare substrates for the exfoliation of $\mathbf{WS_2}$ flakes, either Piranha cleaning or a simpler acetone–IPA (isopropyl alcohol) cleaning method was used. Piranha solution was generally avoided due to its hazardous nature and environmental impact. In most cases, the substrates were cleaned by placing them in acetone at $60°C$ on a hot plate for 30 minutes, followed by immersion in IPA at $60°C$ for 10 minutes. After solvent cleaning, the substrates were activated using O_2 plasma to improve surface adhesion and exfoliation quality.

For cleaning substrates that already contained WS_2 flakes, a gentler procedure was required because excessive wet processing can remove the flakes—an issue that was frequently encountered. In this case, the samples were cleaned in acetone at $60°C$ for 20 minutes, followed by a 5-minute rinse in IPA at room temperature. This procedure was also used to remove the hydrophobic layer transferred from PDMS during the flake-transfer process. I would like to acknowledge Dr. Fahrettin Sarcan for providing this method, which significantly improved our results.

After reactive-ion etching (RIE), the resist was removed using 1165 resist remover for 20 minutes at $60°C$ on a hot plate, followed by 10 minutes in acetone and a final rinse in IPA for 2–5 minutes. The samples were then dried carefully and slowly using N_2 to avoid disturbing the flakes.

4.3 Exfoliation

$\mathbf{WS_2}$ flakes were exfoliated from bulk crystals purchased from 2D semiconductor using blue adhesive tape. Blue tape was selected based on less adhesive residue; however, traditional Scotch tape or other, more adhesive tapes are commonly used as well. It is also noted that different types of flakes may exfoliate more effectively with different tapes, and thus no single tape provides a universal solution. After exfoliation, the flakes were transferred onto a PDMS substrate and examined optically under a microscope. The flake thickness was estimated by comparing their optical contrast with previously calibrated thickness values obtained from Dektak profilometry. Additionally, calibration of the camera's field of view enabled flake dimensions to be determined from pixel measurements, allowing for the identification of the largest flakes for further processing. Selected flakes were marked using red or black ink, and each flake was carefully cut using a sharp blade, ensuring that the PDMS was not stretched or disturbed, as this could damage the flakes. The isolated flakes were then transferred onto a glass slide with the PDMS layer, preparing them for deterministic placement onto the desired locations on the target substrate.

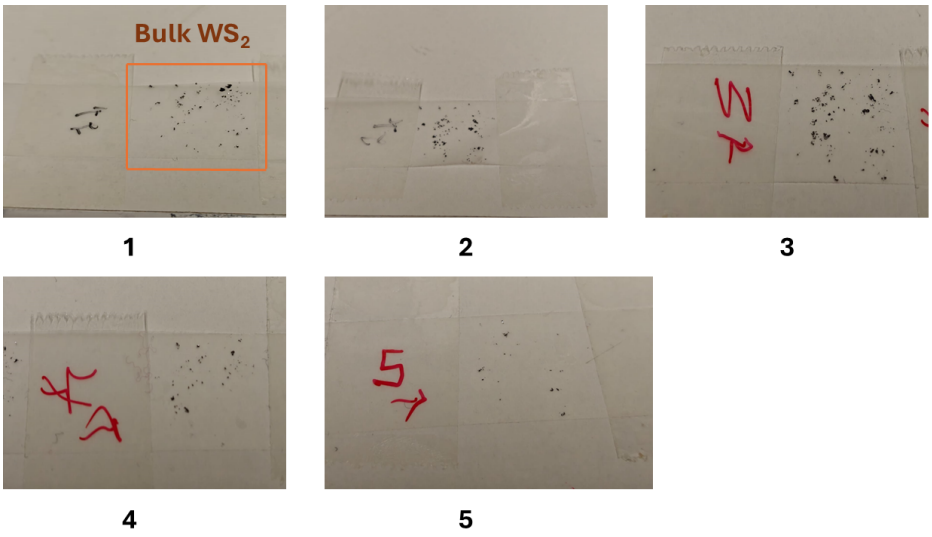

(a) Exfoliation steps shown on sticky tape

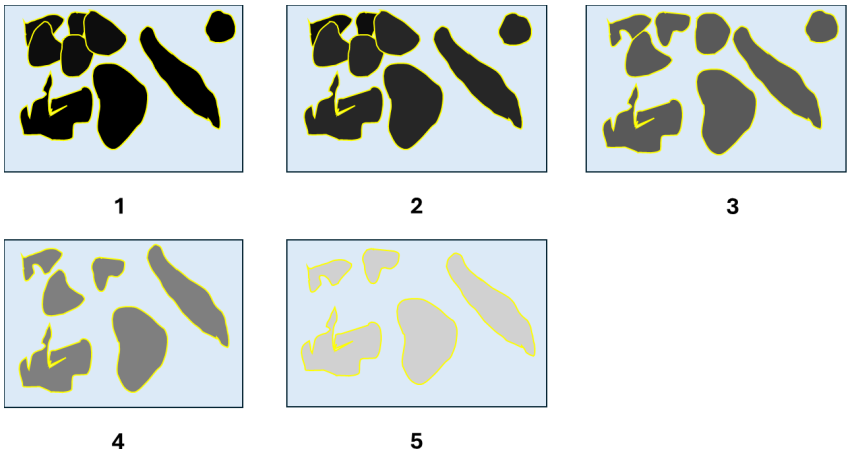

(b) Illustration of exfoliation steps

Figure 4.2: a) Showing exfoliation progress from step 1 to 5. As we Exfoliate from bulk WS_2 crystals, We can see that overall material is reduced and also smaller flakes are found. b) Illustrative representation of a).

4.4 Transfer

The transfer setup is designed to enable precise positioning and alignment of two-dimensional materials onto target substrates. It consists of an optical imaging system integrated with a CCD camera and an optical tube for high-resolution monitoring during the transfer process. A white light source is coupled into the system to provide uniform illumination. The sample is mounted on a heater stage with rotational and translational control, allowing accurate alignment and temperature-assisted transfer. Multiple motorized and manual XYZ stages are incorporated for fine adjustment of both the sample and the imaging components, ensuring stability and precision throughout the process.

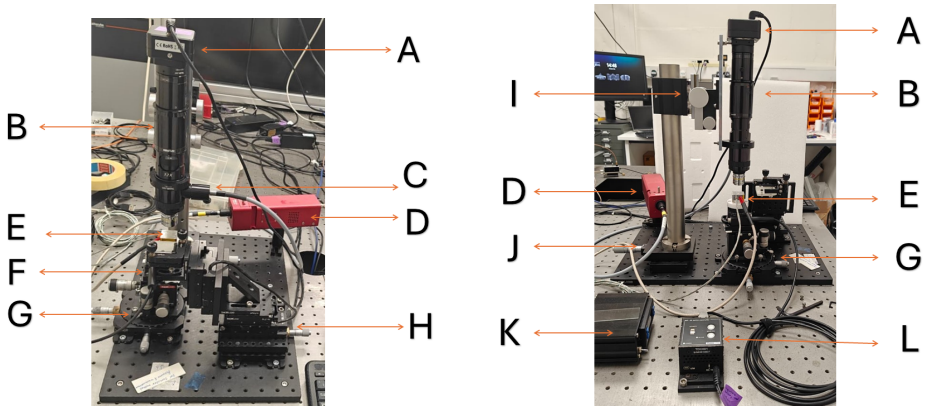

(a) front view of transfer setup (b) side view of transfer setup

Figure 4.3: The front a) and side b) view of the dry transfer setup. A) CCD camera. B) optical telescope. C) Halogen light merging with optical fiber. D) Halogen light source. E) Heater Stage. F) stage rotation. G) X-Y translation stage. H) XYZ stage. I) Movable Z stage. J) XY camera stage. K) Heater Controller. L) rotation controller.

First, a clean substrate is placed on the heater stage. The sample, supported on a glass substrate, is then mounted on the sample holder in an upside-down position, facing towards the substrate on the heater.Using the XY controls of the sample and substrate mounts, along with the Z-control of the camera assembly, the sample is aligned so that it is positioned directly above the desired transfer location.Next, the motorized Z-axis is used to lower the sample onto the substrate. The sample is kept in contact for a few seconds to improve the probability of a successful transfer. The heating stage facilitates a reliable transfer by reducing the stickiness of the PDMS upon heating, thereby enabling the WS_2 crystal to be released more easily. Finally, the sample is slowly lifted, ensuring a clean and reproducible transfer.

4.5 Spin Coating

To achieve a flat and uniform photoresist layer, a spin-coating technique was employed, enabling control of the resist thickness with nanometre-scale precision through adjustments to the spin speed and duration. The positive electron-beam (e-beam) resist AR-P 6200.9, chosen for its high electron-beam sensitivity and strong resistance to plasma etch-

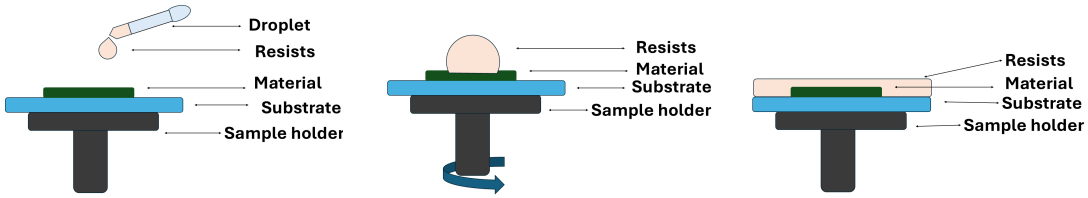

(a) (b) (c)

Figure 4.4: Illustrative representation of the spin-coating process. The resist is first dispensed onto the substrate using a dropper or pipette and then spin-coated to achieve the desired film thickness and uniformity.

ing, was spin-coated at 5000 rpm for one minute and subsequently soft-baked at $120°C$ for two minutes. In standard procedures, an additional conductive layer of AR-PC is applied at 2000 rpm for one minute and baked at $90°C$ for five minutes to mitigate charging effects during e-beam lithography. However, in later experiments this AR-PC layer was omitted, as AR-P 6200.9 alone proved sufficient while also reducing the number of wet-processing steps that could potentially damage the $\mathbf{WS_2}$ flakes. Due to PMMA residue producing a hydrophobic surface on the substrate, achieving a uniform coating on the first attempt was often challenging, and several samples required two to three coating cycles. When an uneven AR-P 6200.9 layer was obtained, it was removed using the 1164 resist remover prior to the baking step.

4.6 Electron-Beam Lithography

Lithography is the process of transferring patterns from one medium to another. For many years, particle beams of various types have been used in lithography. The electron source has the benefit of extremely high diffraction-limited resolution and has been used for transferring patterns having nanometre feature sizes. Recently they have become the popular selection in making nanoscale structures, by both direct writing and projection printing techniques. Electron-beam lithography (EBL) has begun to find applications in direct writing, where the focused beam directly impinges on the resist in order to perform various activities[15].

The definition of nanoscale lithography here follows that provided by the US National Science Foundation, and it can be interpreted as using lithographic tools for fabrication of any structures having feature sizes less than 100 nm. Nanoscale lithography is a large collection of nano-fabrication techniques that have originated from the semiconductor industry. It normally removes or adds material on a substrate[15].

The main advantages of e-beam lithography over the conventional photolithography techniques include very high resolution and versatile pattern formation.The electron de Broglie wavelength of a typical EBL operating condition, 50 keV, is less than 10 pm or 0.01 nm, which is far below typical atomic sizes. Hence, diffraction is not a limiting factor of the resolution. Ideally, e-beam diameters are possible on the order of 1 nm. However, beam-material or scattering interaction degrades this limit significantly [15].

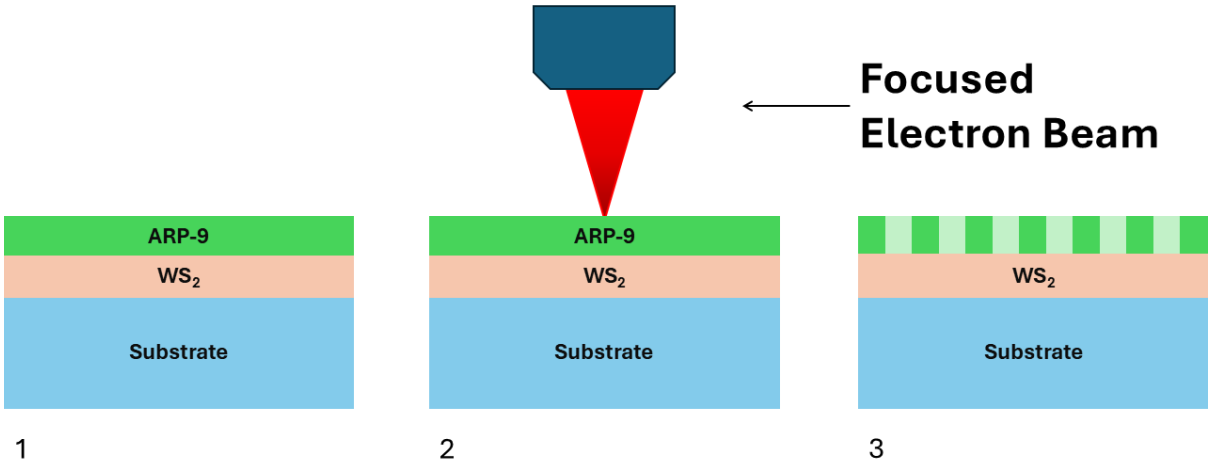

Figure 4.5: Ebeam process

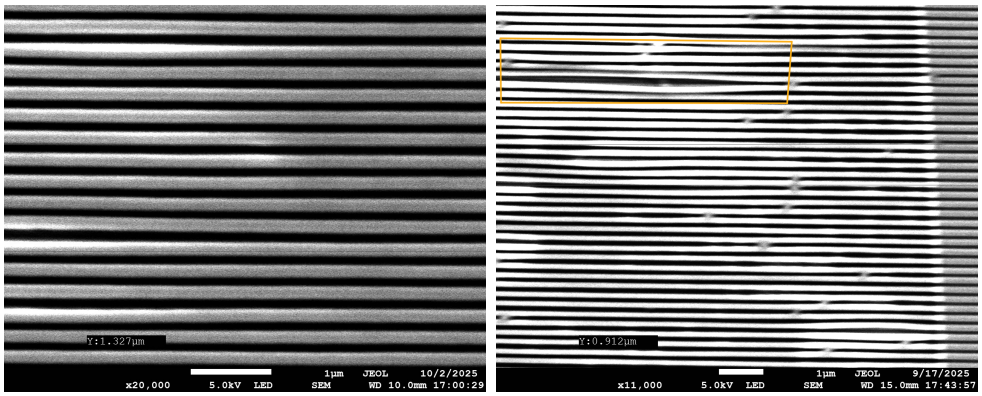

(a) EBL with 160 $\mu C/cm^2$ base Does and 1.0 Does factor.

(b) EBL with 160 $\mu C/cm^2$ base Does and 1.1 Does factor.

Figure 4.6: Scanning electron microscopy (SEM) image of 1D grating in WS_2 after RIE, the sample is coated with an ARP-C layer for charge dissipation.

Scattering or Proximity Effect

When the electron beam strikes the resist solid, many of the electrons experience small-angle forward scattering, which tends to enlarge the initial beam size. As the electrons penetrate through the resist into the substrate, some of them undergo large-angle scattering events leading to backscattering, in which these electrons return back through the resist in a region far from the desired exposure. This causes additional exposure in the resist and is also known as the e-beam proximity effect. Also, as the primary electrons slow down, much of their energy is dissipated in the form of secondary electrons in which a small portion may have significant energies, on the order of 1 keV. These so-called fast electrons are responsible for the bulk of actual resist exposure and can contribute to the proximity effect in the range of a few tenths of a micron [15].

For this project, we used the Raith Voyager EBL system at the University of York, which operates with a 50 kV thermal field emission column for electron-beam generation and includes autofocus and stigmation control. The main parameters that influence the

writing process and resulting feature size are dose, beam current, step size, and dwell time. In this work, only the dose was varied, while the other parameters were kept constant to ensure consistent and reliable results.The base dose can be scaled using a parameter known as the dose factor (DF). A higher dose factor corresponds to a larger number of electrons delivered to the sample, increasing the extent of polymer chain scission in the electron-sensitive resist. In general, increasing the dose leads to greater resist exposure depth, but it can also cause lateral broadening of features (fig4.6b), which must be considered when optimizing lithographic performance. For the optimizing base does several samples were created with low does of 102 $\frac{\mu C}{cm^2}$ to as high as 220 $\frac{\mu C}{cm^2}$.best results were found at 160 $\frac{\mu C}{cm^2}$. keeping the base does and other parameters constant as best as we can all other sample were created.

4.7 Development

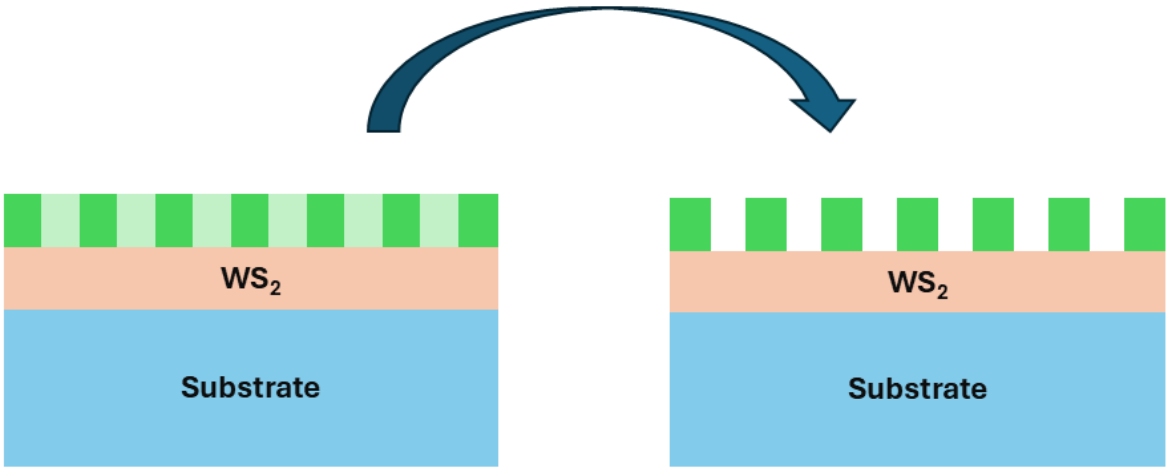

Figure 4.7: Development process

After electron-beam exposure, the charge-dissipation layer (AR-PC) is normally removed using deionised (DI) water. A two-minute DI water submersion followed by DI rinsing is typically sufficient to remove this layer, leaving only the photoresist on the sample surface. The exposed regions of the photoresist are then removed using xylene for two and a half minutes. This process is known as development. Following development, the sample is submerged in isopropanol (IPA) to stop the development in xylene prior to etching[16].

In our recent process, however, the AR-PC layer was not applied; the sample was coated only with AR-P9. As a result, the DI water removal step was unnecessary, instead we performed development directly using xylene, for minute and 45 second, followed by an IPA rinse for two minute. During this stage it is important not to submerge the sample for too long or apply vigorous agitation as $\mathbf{WS_2}$ can detach easily from the substrate, resulting in loos of material and pattern integrity.Figure 4.7 illustrates the overall process flow. During development, xylene selectively dissolves the e-beam-exposed regions of AR-P9, revealing the patterned areas for subsequent etching.

4.8 Reactive Ion Etching

To transfer the pattern from the E-beam resist into the $\mathbf{WS_2}$ layer, a reactive ion etching (RIE) process is employed. RIE is a plasma-based etching technique in which chemically reactive ions are accelerated toward the substrate, enabling material removal through a combination of chemical reactions and physical sputtering. Depending on the required film thickness, surface smoothness, and specific pattern geometry—such as pillars, V-shaped channels, or U-shaped channels—either predominantly chemical (isotropic) or predominantly physical (anisotropic) RIE conditions may be selected. This flexibility allows precise control over etch profiles and enables the fabrication of complex nanoscale structures.

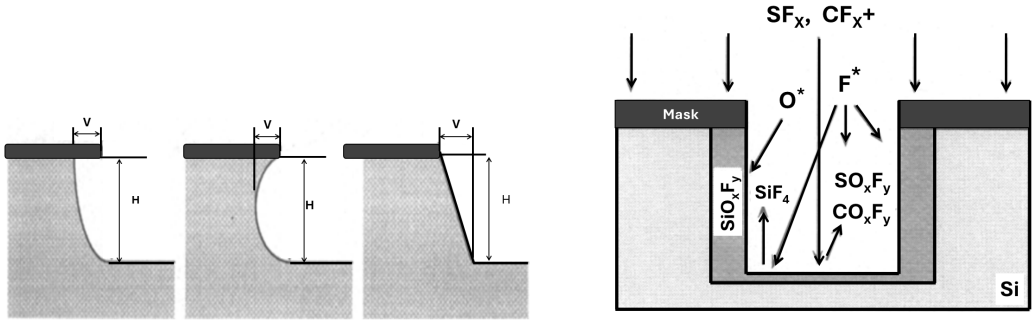

(a) Schematic definition of anisotropy.

(b) Schematic view of the SF_6, O_2, CHF_3, etching process.

Figure 4.8: a) H is etch depth. V is maximal undercut of the mask or in case of outward sloped profiles, the lateral extension of the side well. Reproduced from Legtenberg et al. (1995)[2].

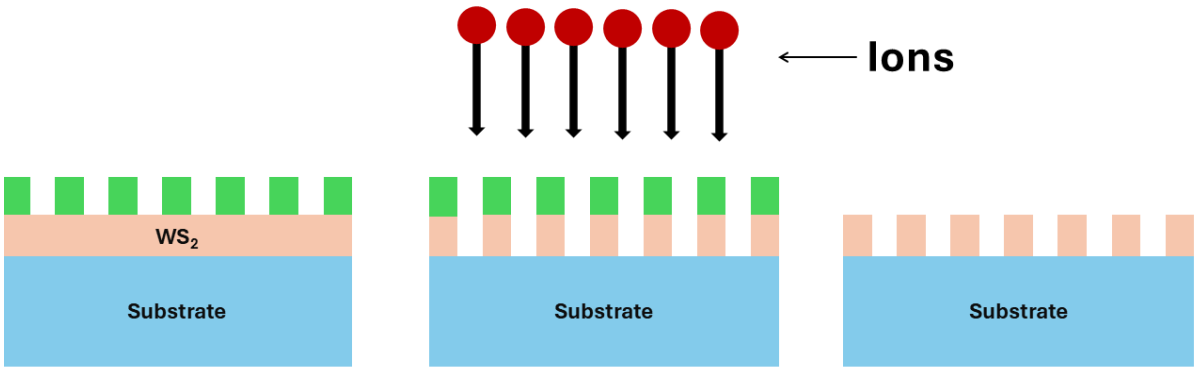

Figure 4.9: RIE process

Anisotropic and **isotropic** reactive ion etching (RIE) are two fundamental etching profiles that play a critical role in micro- and nano fabrication. Isotropic RIE removes material uniformly in all directions, producing rounded or undercut sidewalls due to equal lateral and vertical etch rates. This behaviour typically results from chemistry-dominated processes where reactive neutrals drive the etching and ion directionality plays a smaller role. In contrast, anisotropic RIE achieves highly directional, nearly vertical etch profiles

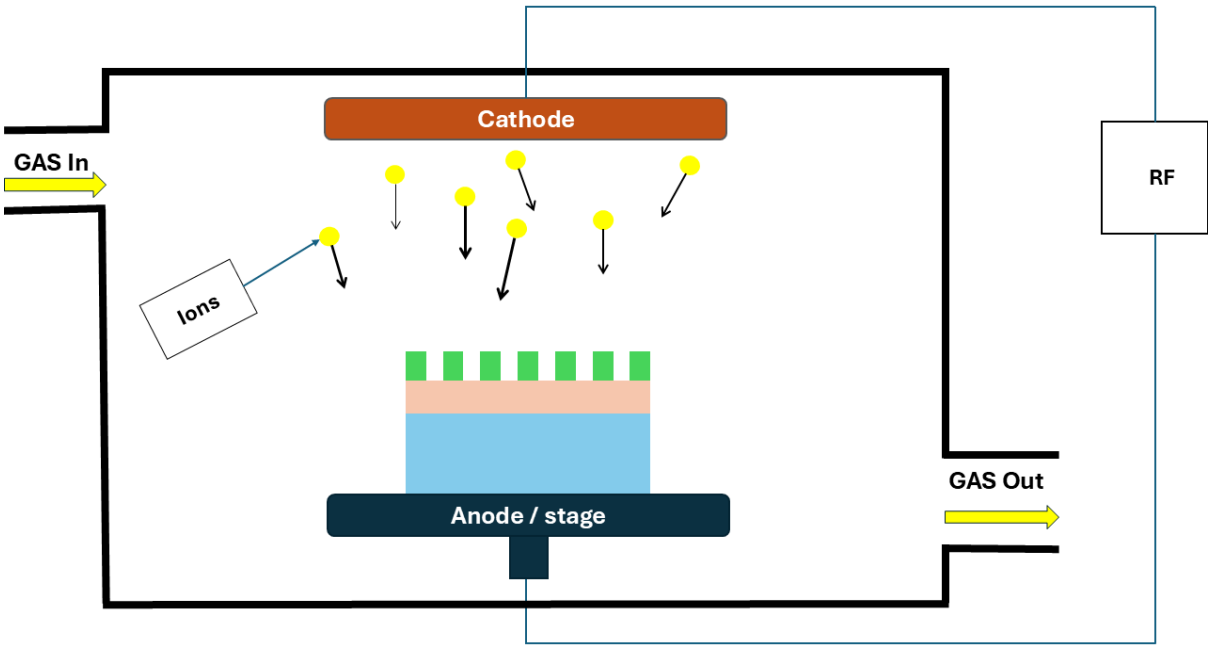

Figure 4.10: Illustration of the RIE Chamber

by combining physical ion bombardment with chemical reactions. The accelerated ions in an RF plasma strike the substrate primarily in the vertical direction, enhancing etch rates downward while suppressing lateral etching. This makes anisotropic RIE essential for fabricating high-aspect-ratio features, precise pattern transfer, and device structures requiring dimensional accuracy. Understanding the balance between chemical reactivity, ion energy, pressure, and plasma composition is crucial for tailoring etch profiles and selecting between isotropic and anisotropic modes depending on the desired device architecture.

The plasma is initiated by the application of a 13.56MHz RF powered electrode (cathode). The electric field ionises the gas molecules to create the plasma. A DC bias voltage forms on the bottom of the RF-powered electrode, extracting ions from the 'bulk' plasma, thus the DC bias contributes to the directionality of etching the sample.

In this experiment, an 1D grating of $\mathbf{WS_2}$ sample was processed in a plasma etching chamber similar to that shown in Figure 4.10. Prior to etching, the chamber was conditioned using two cleaning steps while maintaining a constant gate position. First, a hydrogen clean was carried out with a gas flow of 20 sccm Ar + 10 sccm H_2, operated at 40 W RF power and a 400 V DC bias, resulting in a measured pressure of 3×10^{-2} Torr for a duration of 5 minutes. This was followed by an oxygen clean using 30 sccm O_2 at 59 W power, a 500 V DC bias, and a measured pressure of 4.8×10^{-2} Torr, also for 5 minutes. After chamber conditioning, the sample was etched using a mixture of 14.5 sccm CHF_3 and 12.5 sccm SF_6 (ratio 1.16:1). The etching was performed at 27 W RF power and a 135 V DC bias, with the gate position held constant and a resulting measured pressure of 1.3Ö10^{-1} Torr. A 5-minute pre-plasma step was employed to promote chemical activation prior to etching. This was followed by a 35-second etch, which was sufficient to remove the photoresist and produce the desired periodic array through the AR-P9 layer and into the $\mathbf{WS_2}$.

4.9 Scanning Electron Microscopy

The SEM system used in this work is the JEOL 7800F Prime SEM, located in the York JEOL Nanocentre.

Charge accumulation also presented challenges during electron microscopy imaging. To mitigate this, an additional charge-dissipation layer was applied. For imaging purposes, this layer must be as thin as possible; therefore, a 5–10 nm coating of AR-PC was deposited using the spin-coating method. Although we also evaluated a thin copper (Cu) layer for charge dissipation, its use was ultimately avoided because it cannot be removed from the sample, rendering the specimen unsuitable for further experimentation. Despite its removability, AR-PC did not fully eliminate charging effects, and in combination with the underlying AR-P9 layer, it contributed to slight structural expansion. Consequently, low beam voltages were generally employed during imaging to minimize charging and preserve structural integrity.

Chapter 5

Optical Characterisation Result

5.1 Optical Characterisation

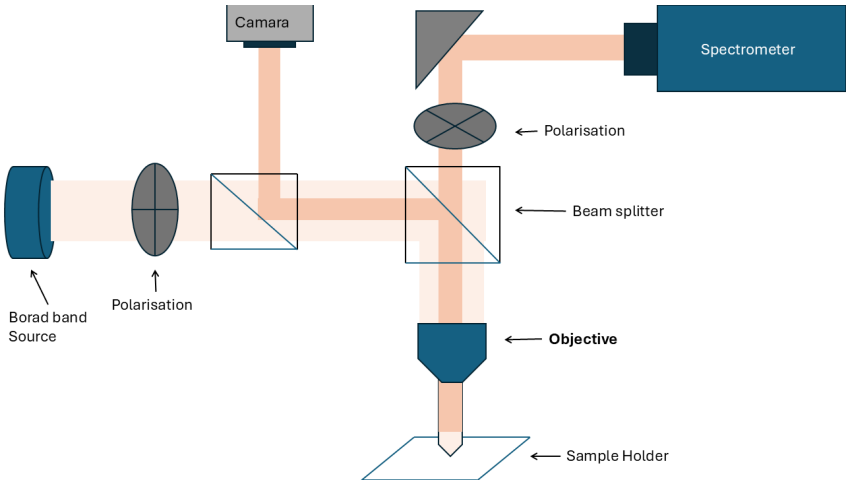

Figure 5.1: Reflection measurement setup.

Figure 5.1 shows a schematic of the reflection-measurement setup. The system consists of two polarisers—one positioned at the beginning of the optical path and the second at the end. The first polariser sets the incident polarization, either perpendicular or parallel to the grating, ensuring that the incoming light is well-defined with respect to the grating orientation. The sample holder is capable of movement in all three spatial directions (x, y, and z), allowing precise focusing on the grating. A camera is used to align the grating, while the objective lens focuses the light and, together with an additional lens, produces a non-diverging beam.

Light from the halogen bulb source is delivered to the setup via an optical fiber, after which it passes through the first polarizer and then through the focusing lens. This lens directs the light to the back focal plane (BFP) of the objective, allowing it to be focused onto the sample. The reflected light travels back through the objective and is then directed through a beam splitter. One arm of the beam splitter leads to the camera for imaging and alignment, while the other directs the light to the spectrometer. The

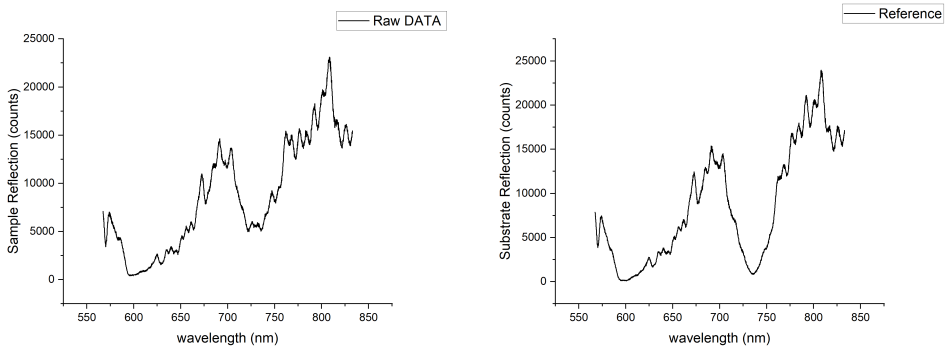

Figure 5.2: Raw data from spectrometer measurement. Left is measured on the GMR structure and right is measured on substrate.

spectrometer contains interchangeable gratings that can be selected to adjust sensitivity and spectral resolution depending on the specific measurement requirements.

The measured spectra require further processing in order to extract meaningful optical characteristics. This is achieved by normalizing the measured reflection spectrum of the sample using a reference reflection spectrum of the light source. Ideally, this reference should be obtained using a mirror with near-perfect reflectivity, such as a gold-coated mirror. The reflection spectrum from the one-dimensional (1D) grating is then referenced by dividing it by the mirror reflection spectrum.

This normalization compensates for non-idealities in the optical system, including the non-uniform polarization state of the source. In particular, the incident beam is not perfectly circularly polarized, and the vertical (TE) polarization component is stronger than the horizontal (TM) component. By referencing the sample spectrum to the mirror spectrum, these source-related and system-dependent effects are effectively minimized.

However, due to spatial constraints in the setup and to avoid disturbing the axial (z-axis) focus of the optical components, a reference mirror could not be introduced. Instead, the bare substrate was used as the reference. While this approach does not provide an ideal normalization due to the substrate's non-unity reflectivity, it still allows for a consistent and practical comparison of the measured spectra.

As a result of this normalization procedure, the reflection spectra are presented in arbitrary units (A.U.), since the measured signal represents a relative intensity referenced to a reflection standard rather than an absolute reflectance. The spectrometer records detector counts that depend on system-specific factors such as source power, fiber coupling efficiency, detector sensitivity, and optical losses, which are not independently calibrated. Consequently, absolute reflectivity cannot be directly obtained; however, expressing the data in A.U. enables consistent comparison of spectral features such as resonance positions, line widths, and relative intensity variations—across different measurements and polarization conditions, which is sufficient for analyzing the optical response of the grating.

5.2 Results

As discussed in Section 3.3, the initial design parameters for fabrication were a grating period of 200 nm and a fill factor of 80 %, corresponding to a WS_2 grating widthw_g of 160 nm and a gap width W_r of 40 nm, as illustrated in Fig. 3.2 and Fig. 3.1. However, dose-test measurements revealed that a lithography dose of 160 $\frac{\mu C}{cm^2}$ resulted in an actual ridge width of approximately 90 nm. This value was subsequently confirmed through SEM imaging. Based on these findings, a new set of simulations was performed to identify an optimized grating design that reflects the experimentally obtained ridge width. In this updated simulation series, the ridge width was fixed at 90 nm, while the grating period was varied to determine the period–fill-factor combinations that yield improved device performance.

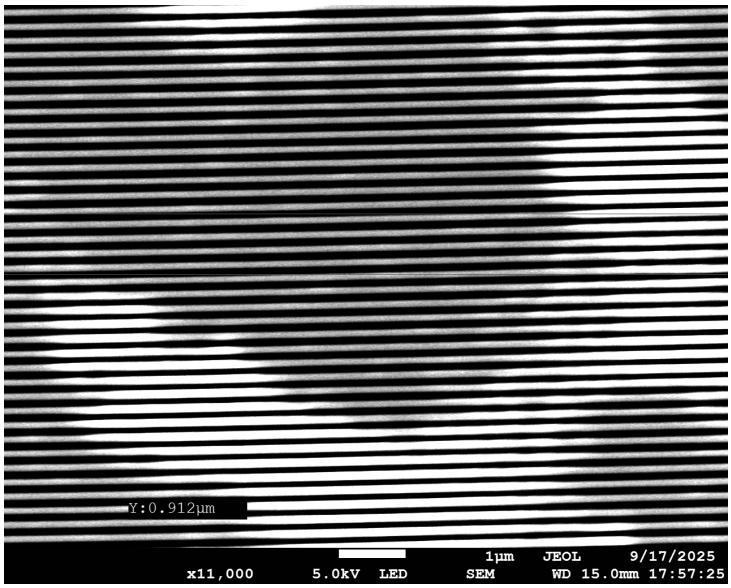

Figure 5.3: SEM image of 1D grating of WS_2 with EBL Dose 160 $\frac{\mu C}{cm^2}$. The measured period of structure is 220 nm.

To achieve simulation results that more accurately represent the fabricated structure, wavelength-dependent refractive index and absorption parameters were incorporated into the model. Specifically, wavelength-dependent absorption coefficients were applied to both WS_2 and Si, while wavelength-dependent refractive indices were used for WS_2, SiO_2 and Si. The corresponding material data, extracted from literature, are provided in graphical form in Appendix 6.2 (Fig. 6.1, Fig. 6.2, and Fig. 6.3), all the DATA were taken from online tool "Refractiveindex.info database of optical constants" [17].

Based on the simulation transmission response shown in fig. 5.4, the optimal grating period was found to lie in the range of 265-285nm. For a period of 265nm, the geometry corresponding to gap width $W_r = 94$nm, a grating width $W_g = 171$nm and a fill factor of 64.5%.The spectral response for this configuration was subsequently measured and analysed. For a grating period of 265 nm, a peak wavelength of 690 nm was observed, while for a period of 280 nm, a peak wavelength of 722 nm was found.

Figures 5.5–5.7 show the measured reflection spectra for structures with different grating periods. It is important to consider potential sources of measurement error when

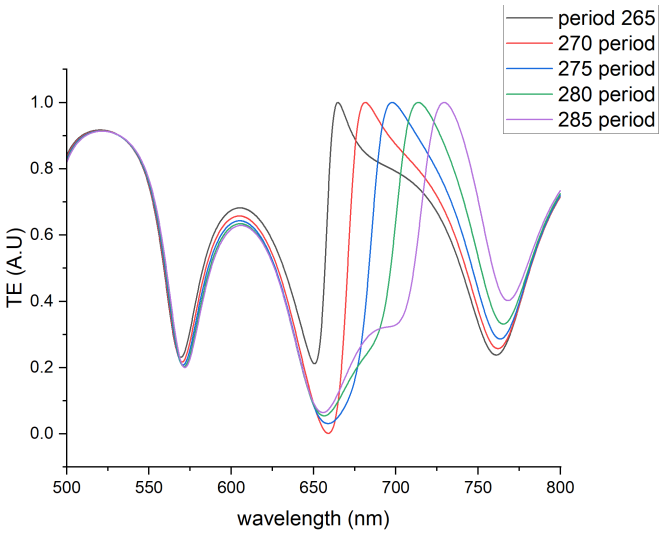

Figure 5.4: Simulation result for finding new period with constrain of fabrication. This simulation was done with wavelength depend values of reflective index n and extinction coefficient k of materials for the period of 265 nm to 285 nm.

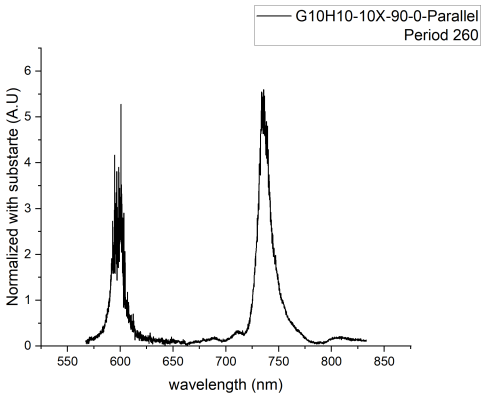

Figure 5.5: Reflection spectrum measured from a grating with of period of 260 nm. The unit of normalized reflection is in arbitrary unit.

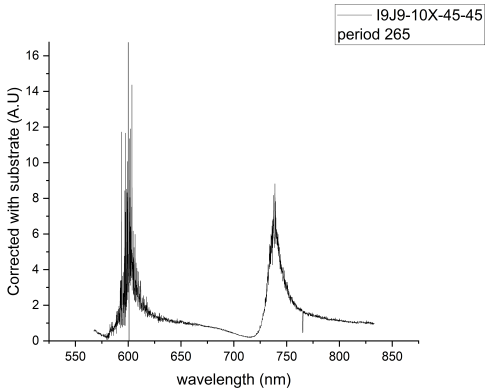

Figure 5.6: Reflection spectrum measured from a grating with of period of 265 nm. The unit of normalized reflection is in arbitrary unit.

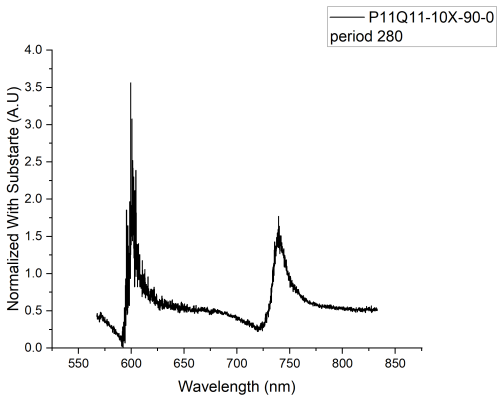

Figure 5.7: Reflection spectrum measured from a grating with of period of 280 nm. The unit of normalized reflection is in arbitrary unit

interpreting these results. From these figures, it is evident that some of the spectral variations arise from experimental uncertainty rather than physical changes in the structures themselves.

In particular, the spectrum for the 265 nm-period structure (Figure 5.6) exhibits more noise and a less stable signal compared to the other measurements. This increased noise is likely due to the sample flakes being rotated by approximately 45 Degree on the substrate. Such a misalignment can cause simultaneous coupling to both TE and TM modes during the measurement, thereby introducing additional features and instability in the recorded spectrum.

The left-side peak observed in all measurements originates primarily from absorption in the Si substrate and the WS_2 layer, as well as from reflection contributions from the SiO_2 layer. A detailed analysis of these substrate-related effects lies outside the scope of this thesis; however, they are worth investigating in future work. Notably, similar behaviour appears in the numerical simulations, which also show a feature around 600 nm (fig 5.4).Across all measured spectra, the TE mode consistently appears stronger than the TM mode. This is expected for this grating configuration and further supports the interpretation that the primary resonance features are correctly captured despite measurement variations.

The optical measurement results of these structures are summarized as follows: for a grating period of 260 nm, a peak wavelength of 736 nm with a Q-factor of 46 was observed. For a period of 265 nm, the peak wavelength was 740 nm with a Q-factor of 46, while for a period of 280 nm, the peak wavelength was 742 nm, also with a Q-factor of 46.

From the simulation results shown in Fig. 5.4, the peak wavelength for a period of 265 nm was 690 nm, and for a period of 280 nm it was 722 nm. Although there is an offset between the simulated and experimental peak positions, both approaches exhibit a clear and consistent trend of red-shifting wavelength with increasing grating period.

All peak wavelengths and Q-factors were extracted using Gaussian fitting of the spectra in Origin software to ensure consistency across all measurements.

Chapter 6

Conclusion and Future work

6.1 Conclusion

In this work, we successfully fabricated and optically characterized one-dimensional grating nanostructures in two-dimensional WS_2 materials. A complete fabrication workflow was developed, encompassing exfoliation, deterministic transfer, electron-beam lithography, development, and reactive ion etching. Using this process, gratings with multiple periods were reliably produced and subsequently characterized using scanning electron microscopy (SEM) and optical reflection spectroscopy.

The fabricated structures exhibited clear optical resonances, with measured Q-factors of 46 for a grating period of 260 nm, 46 for 265 nm, and 46 for 280 nm. An optimized electron-beam lithography base dose of 160 $\frac{\mu C}{cm^2}$ was identified as critical for achieving consistent feature definition and reproducible grating dimensions. SEM analysis confirmed the fabricated periods and fill factors, showing good agreement with the intended designs and demonstrating an estimated dimensional accuracy of approximately 1–3%, despite residual charging effects associated with AR-PC coatings.

Comparison between experimental measurements and numerical simulations showed good agreement. Although a systematic offset was observed between simulated and measured resonance wavelengths, both approaches exhibited a clear and consistent red-shift of the resonance with increasing grating period. This agreement confirms that the dominant physical mechanisms governing the optical response are well captured by the simulations, particularly when wavelength-dependent refractive index and absorption parameters were incorporated into the model. The remaining discrepancies are likely attributable to fabrication tolerances, material inhomogeneity, substrate effects, and experimental limitations in absolute reflectivity measurements.

Throughout the project, several practical challenges were encountered, including flake detachment during wet processing, non-uniform resist coating, proximity effects in electron-beam lithography, and charging during SEM imaging. These issues were systematically addressed through process optimization, such as modifying cleaning procedures, refining resist application, and carefully selecting imaging conditions. In addition to advancing

the fabrication process, this work provided valuable hands-on experience with advanced nano fabrication and characterization tools, including EBL, SEM, RIE, and optical spectroscopy.

Overall, this study demonstrates that high-quality WS_2 grating nanostructures can be fabricated reproducibly using electron-beam lithography and that their optical responses can be reliably measured and correlated with numerical simulations. The results highlight the potential of patterned two-dimensional materials for nanoscale photonic applications while also identifying clear pathways for further refinement and future development.

6.2 Future work

While the present study successfully demonstrates the fabrication and optical characterization of WS_2 grating nanostructures, several avenues remain for future exploration to further enhance device performance and understanding. Future research can focus on further optimization of the fabrication process to improve the fidelity and uniformity of WS_2 grating nanostructures. This includes fine-tuning electron-beam lithography parameters, reactive ion etching conditions, and charge-dissipation strategies during imaging, which could enhance structural accuracy and reduce potential damage to the flakes. Exploring alternative 2D materials or heterostructures may also enable new optical resonances and broaden the applicability of these devices.

Additionally, extending the optical characterization to include angle-resolved, polarization-resolved, or absolute reflectivity measurements could provide deeper insights into the light–matter interactions and resonance behaviour of the gratings. Integrating these structures into photonic platforms, such as waveguides, cavities, or meta-surfaces, presents opportunities to study enhanced optical functionalities and device-level performance.

Finally, scaling up the fabrication to larger areas or arrays and assessing reproducibility across multiple samples will be essential for practical applications. These directions will not only refine the understanding of WS_2 nanostructures but also lay the groundwork for their integration into advanced photonic and optoelectronic devices.

Bibliography

[1] Manuel Deckart. *Guided Mode Resonance Enhanced Microscopy and Lasing*. Doctor of philosophy, University of York, 2023.

[2] Rob Legtenberg, Henri Jansen, Meint de Boer, and Miko Elwenspoek. Anisotropic reactive ion etching of silicon using sf6/o2/chf3 gas mixtures. *Journal of The Electrochemical Society*, 142(6):2020–2028, June 1995.

[3] Kostya S Novoselov, Andre K Geim, Sergei V Morozov, De-eng Jiang, Yanshui Zhang, Sergey V Dubonos, Irina V Grigorieva, and Alexandr A Firsov. Electric field effect in atomically thin carbon films. *science*, 306(5696):666–669, 2004.

[4] K S Novoselov, Artem Mishchenko, Alexandra Carvalho, and AH Castro Neto. 2d materials and van der waals heterostructures. *Science*, 353(6298):aac9439, 2016.

[5] Luojun Du, Maciej R Molas, Zhiheng Huang, Guangyu Zhang, Feng Wang, and Zhipei Sun. Moiré photonics and optoelectronics. *Science*, 379(66392):eadg0014, 2023.

[6] F. Javier García de Abajo, D. N. Basov, Frank H. L. Koppens, Lorenzo Orsini, Matteo Ceccanti, Sebastián Castilla, Lorenzo Cavicchi, Marco Polini, P. A. D. Gonçalves, A. T. Costa, N. M. R. Peres, N. Asger Mortensen, Sathwik Bharadwaj, Zubin Jacob, P. J. Schuck, A. N. Pasupathy, Milan Delor, M. K. Liu, Aitor Mugarza, Pablo Merino, Marc G. Cuxart, Emigdio Chávez-Angel, Martin Švec, Luiz H. G. Tizei, Florian Dirnberger, Hui Deng, Christian Schneider, Vinod Menon, Thorsten Deilmann, Alexey Chernikov, Kristian S. Thygesen, Yohannes Abate, Mauricio Terrones, Vinod K. Sangwan, Mark C. Hersam, Leo Yu, Xueqi Chen, Tony F. Heinz, Puneet Murthy, Martin Kroner, Tomasz Smolenski, Deepankur Thureja, Thibault Chervy, Armando Genco, Chiara Trovatello, Giulio Cerullo, Stefano Dal Conte, Daniel Timmer, Antonietta De Sio, Christoph Lienau, Nianze Shang, Hao Hong, Kaihui Liu, Zhipei Sun, Lee A. Rozema, Philip Walther, Andrea Alù, Andrea Marini, Michele Cotrufo, Raquel Queiroz, X.-Y. Zhu, Joel D. Cox, Eduardo J. C. Dias, Álvaro Rodríguez Echarri, Fadil Iyikanat, Paul Herrmann, Nele Tornow, Sebastian Klimmer, Jan Wilhelm, Giancarlo Soavi, Zeyuan Sun, Shiwei Wu, Ying Xiong, Oles Matsyshyn, Roshan Krishna Kumar, Justin C. W. Song, Tomer Bucher, Alexey Gorlach, Shai Tsesses, Ido Kaminer, Julian Schwab, Florian Mangold, Harald Giessen, M. Sánchez Sánchez, D. K. Efetov, T. Low, G. Gómez-Santos, T. Stauber, Gonzalo Álvarez Pérez, Jiahua Duan, Luis Martín-Moreno, Alexander Paarmann, Joshua D. Caldwell, Alexey Y. Nikitin, Pablo Alonso-González, Niclas S. Mueller, Valentyn Volkov, Deep Jariwala, Timur Shegai, Jorik van de Groep, Alexandra Boltasseva,

Igor V. Bondarev, Vladimir M. Shalaev, Jeffrey Simon, Colton Fruhling, Guangzhen Shen, Dino Novko, Shijing Tan, Bing Wang, Hrvoje Petek, Vahagn Mkhitaryan, Renwen Yu, Alejandro Manjavacas, J. Enrique Ortega, Xu Cheng, Ruijuan Tian, Dong Mao, Dries Van Thourhout, Xuetao Gan, Qing Dai, Aaron Sternbach, You Zhou, Mohammad Hafezi, Dmitrii Litvinov, Magdalena Grzeszczyk, Kostya S. Novoselov, Maciej Koperski, Sotirios Papadopoulos, Lukas Novotny, Leonardo Viti, Miriam Serena Vitiello, Nathan D. Cottam, Benjamin T. Dewes, Oleg Makarovsky, Amalia Patanè, Yihao Song, Mingyang Cai, Jiazhen Chen, Doron Naveh, Houk Jang, Suji Park, Fengnian Xia, Philipp K. Jenke, Josip Bajo, Benjamin Braun, Kenneth S. Burch, Liuyan Zhao, and Xiaodong Xu. Roadmap for photonics with 2d materials. *ACS Photonics*, 12(8):3961–4095, 2025.

[7] Giorgio Quaranta, Guillaume Basset, Olivier J. F. Martin, and Benjamin Gallinet. Recent advances in resonant waveguide gratings. *Laser & Photonics Reviews*, 12, 2018.

[8] John D. Joannopoulos, Steven G. Johnson, Joshua N. Winn, and Robert D. Meade. *Photonic Crystals: Molding the Flow of Light - Second Edition*. Princeton University Press, rev - revised, 2 edition, 2008.

[9] John David Jackson. *Classical electrodynamics*. Wiley, New York, (NY), 3rd ed. edition, 1999.

[10] A. J. Ward and J. B. Pendry. Refraction and geometry in maxwell's equations. *Journal of Modern Optics*, 43:773–793, 1996.

[11] Katsunari Okamoto. *Fundamentals of Optical Waveguides*. Academic Press, 3rd edition, 2006.

[12] Felix Bloch. Uber die quantenmechanik der elektronen in kristallgittern. *Zeitschrift fur Physik*, 52(7-8):555–600, jul 1929.

[13] Victor Liu and Shanhui Fan. S^4 : A free electromagnetic solver for layered periodic structures. *Computer Physics Communications*, 183(10):2233 – 2244, 2012.

[14] Manfred Hammer. 1-d mode solver for dielectric multilayer slab waveguides.

[15] A.A. Tseng, Kuan Chen, C.D. Chen, and K.J. Ma. Electron beam lithography in nanoscale fabrication: recent development. *IEEE Transactions on Electronics Packaging Manufacturing*, 26(2):141–149, 2003.

[16] Joshua S. Male. *Thermally Enhanced Paper Microfluidics for Photonic Crystal Biosensors in Amorphous Silicon*. Master of science by research, University of York, 2019.

[17] M. N. Polyanskiy. Refractiveindex.info database of optical constants. *Scientific Data*, 11:94, 2024.

[18] A. A. Vyshnevyy, G. A. Ermolaev, D. V. Grudinin, K. V. Voronin, I. Kharichkin, A. Mazitov, I. A. Kruglov, D. I. Yakubovky, P. Mishra, R. V. Kirtaev, A. V. Arsenin, K. S. Novoselov, L. Martin-Moreno, and V. S. Volkov. Van der waals materials for overcoming fundamental limitations in photonic integrated circuitry. *Nano Letters*, 23:8057 – 8064, 2023.

[19] I. H. Malitson. Interspecimen comparison of the refractive index of fused silica∗,†. *J. Opt. Soc. Am.*, 55(10):1205–1209, Oct 1965.

[20] D. E. Aspnes and A. A. Studna. Dielectric functions and optical parameters of si, ge, gap, gaas, gasb, inp, inas, and insb from 1.5 to 6.0 ev. *Phys. Rev. B*, 27:985–1009, Jan 1983.

Appendix

Material Information

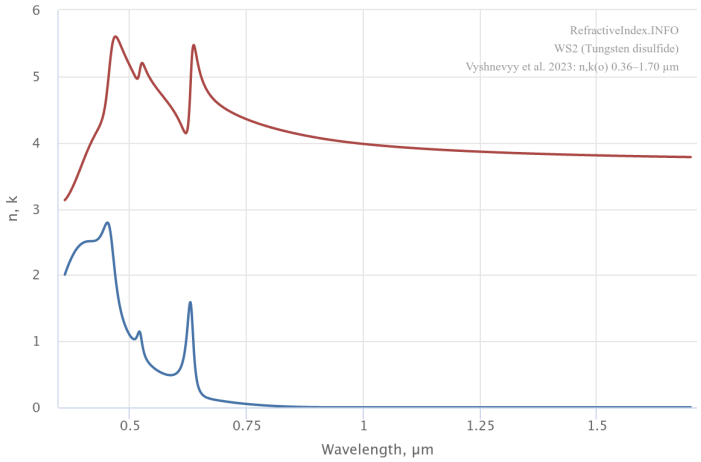

Figure 6.1: WS_2 n and k info

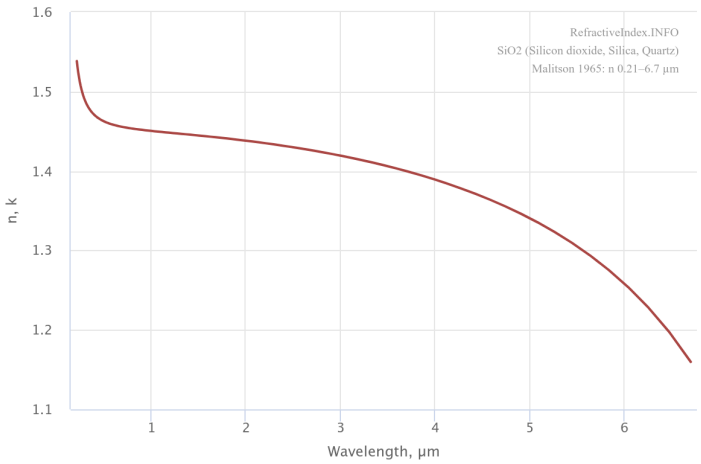

Figure 6.2: SiO_2 n and k info

All the material data used in this thesis is taken from online tool[17]. where original data is from individual research papers, WS_2[18], SiO_2[19] and Si [20].

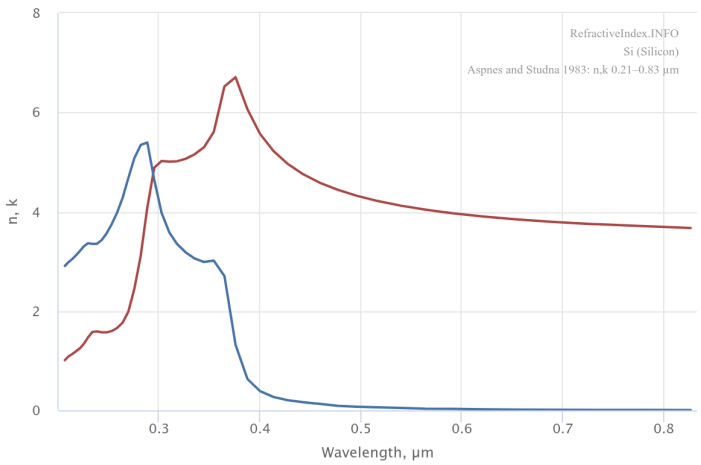

Figure 6.3: Si n and k info